

See discussions, stats, and author profiles for this publication at: <https://www.researchgate.net/publication/263324073>

# Spheroids in Viscoplastic Fluids: Drag and Heat Transfer

ARTICLE *in* INDUSTRIAL & ENGINEERING CHEMISTRY RESEARCH · JUNE 2014

Impact Factor: 2.59 · DOI: 10.1021/ie501256v

---

CITATIONS

3

---

READS

62

## 1 AUTHOR:



Anoop Kumar Gupta

Indian Institute of Technology Kanpur

7 PUBLICATIONS 12 CITATIONS

[SEE PROFILE](#)

# Spheroids in Viscoplastic Fluids: Drag and Heat Transfer

Anoop Kumar Gupta and R. P. Chhabra\*

Department of Chemical Engineering, Indian Institute of Technology Kanpur, Nankari, Kalyanpur, Kanpur, Uttar Pradesh 208016, India

## Supporting Information

**ABSTRACT:** In the present work, the forced convection momentum and heat transfer aspects of isothermal spheroidal particles (both prolates and oblates) in Bingham plastic fluids have been numerically investigated in the steady axisymmetric flow regime. Extensive results on the detailed structures of the flow and temperature fields are presented and analyzed in terms of the streamline and isotherm contours, and the yield surfaces as well as their dependence on the pertinent influencing parameters, namely, Reynolds number ( $1 \leq Re \leq 100$ ), Prandtl number ( $1 \leq Pr \leq 100$ ), and Bingham number ( $0 \leq Bn \leq 100$ ) are delineated. Five values of aspect ratio,  $e = 0.2$  and  $0.5$  (oblates) and  $e = 2$  and  $5$  (prolates), and the limiting case of a sphere, i.e.,  $e = 1$ , are considered here to elucidate the effect of shape on both drag and Nusselt number values. Broadly, for a given shape (value of  $e$ ), drag shows the classic inverse dependence on the Reynolds number and a positive correlation with the Bingham number. Similarly, the mean Nusselt number bears a positive dependence on each of these parameters,  $Re$ ,  $Pr$ , and  $Bn$ , due to the sharpening of the temperature gradient in the thin thermal boundary layer. The present drag results have been correlated via the use of a modified Reynolds number whereas the heat transfer results have been consolidated in terms of the Colburn  $j_H$  factor, thereby enabling their prediction in a new application.

## 1. INTRODUCTION

Due to the wide occurrence of viscoplastic fluid behavior in a broad spectrum of industrial settings,<sup>1–3</sup> significant research efforts have been expended in elucidating the influence of fluid yield stress on the convective momentum and heat transport in a range of geometries of practical and fundamental interest, such as in duct flows,<sup>1,4,5</sup> porous media flows,<sup>6,7</sup> batch mixing vessels,<sup>8,9</sup> etc. On the other hand, much less is known about the analogous external boundary layer-type flows, especially for axisymmetric shaped objects such as prolates and oblates. Admittedly there exists a sizable body of knowledge on the flow past single spheres in Bingham and Herschel–Bulkley model viscoplastic fluids; for example, see refs 10–14 for numerical results and refs 15–19 for experimental results. While the preceding numerical studies relate to the case of flow past fixed spheres, the corresponding reverse problem of settling spheres has been considered by Prashant and DerkSEN<sup>20</sup> and Yu and Wachs<sup>21</sup> by using the direct simulation and the fictitious domain approaches, respectively. It is fair to add here that most of these studies are aimed at developing the stability criterion (whether a given sphere of known weight will fall under gravity in a fluid of given yield stress), drag correlations, and wall effects and ascertaining the size and shape of the yield surfaces in the creeping flow regime (vanishingly small values of the particle Reynolds number). Indeed, these creeping flow studies have been extended to finite Reynolds numbers ( $Re \leq 100$ ) only recently<sup>13,14</sup> wherein the first set of numerical results on the Nusselt number in the forced convection regime were also reported. Suffice it to say here that the available experimental results on the drag and size/shape of the yield surfaces are consistent with the numerical predictions, in both the creeping and finite Reynolds number regimes. On the other hand, for a given Reynolds number, there exists a limiting Bingham number beyond which no yielding occurs and the resulting

values of the Nusselt number under these conditions approach the expected conduction limit. Furthermore, while corresponding results on the forced convection heat transfer from circular<sup>22</sup> and elliptical cylinders<sup>23</sup> are also available and corroborate the existence of such limiting Bingham numbers, beyond which heat transfer occurs purely by conduction. In contrast, very little is known about the effect of the particle shape of solids of revolution on the drag and heat transfer in viscoplastic fluids. One convenient shape to explore this aspect is that of spheroid. By simply varying the aspect ratio and/or the axis of rotation, it is possible to span wide ranges of particle shapes, prolates, and oblates, which are all free from geometrical singularities. This work is concerned with the study of drag and Nusselt number characteristics of spheroids, both oblates and prolates, particles in Bingham plastic fluids in the steady axisymmetric flow regime.

Over the years, numerous analytical, numerical, and experimental studies dealing with the drag and Nusselt number characteristics and wall effects for single and multiple spheroids in Newtonian fluids have been reported in the literature. The bulk of these studies have been reviewed, among others, by Clift et al.<sup>24</sup> in their classic treatise, and more recently by Michaelides<sup>25</sup> and Kishore and co-workers.<sup>26–29</sup> All in all, the currently available numerical simulations in this field are generally limited to the axisymmetric flow regime, and scant experimental results are consistent with these predictions.<sup>30</sup> The next generation of developments in this field have dealt

**Special Issue:** Ganapati D. Yadav Festschrift

**Received:** March 25, 2014

**Revised:** June 2, 2014

**Accepted:** June 3, 2014



with the prediction of the drag and Nusselt number for oblates and prolates in power-law fluids.<sup>31–33</sup> Not only are these numerical results restricted to the axisymmetric flow regime, but there are no experimental results available to substantiate or refute the numerical predictions of drag on prolates and oblates in power-law fluids. In a nutshell, at low Reynolds numbers, shear-thinning power-law viscosity tends to augment the drag over and above that in Newtonian fluids whereas the effect of power-law index progressively diminishes with increasing Reynolds number due to the increasing dominance of inertial effects over viscous effects. On the other hand, in the forced convection regime, shear-thinning power-law viscosity promotes the rate of heat transfer with reference to that in Newtonian fluids.<sup>33</sup> Both these trends are qualitatively similar to that for a sphere in power-law fluids.<sup>34–38</sup>

In spite of the frequent occurrence of viscoplastic fluid behavior in the thermal treatment of various food stuffs, in the manufacture of health- and personal-care products, and in the formulation of synthetic drilling muds, etc., to the best of our knowledge, no prior results are available on the settling velocity (drag) and Nusselt number for prolates and oblates in such fluids. One of the key features in the flow of such substances is the simultaneous coexistence of yielded (fluid-like) and unyielded (solid-like) regions in the flow domain depending upon the magnitude of the local stress tensor in the fluid vis-a-vis the fluid yield stress. Naturally, heat transfer will occur by convection only in the yielded regions whereas conduction will be the dominant mode of heat transfer in the unyielded parts of the material. This can thus directly influence the overall rate of heat transfer and temperature distribution in such a system. This work endeavors to fill this gap in the literature by numerically studying the effect of a particle shape on the yield surfaces and hence on the drag and heat transfer aspects.

In particular, the momentum and thermal energy equations describing the flow and heat transfer from a spheroid in Bingham plastic fluids have been solved numerically to delineate the influence of the pertinent parameters, namely, Reynolds number ( $Re$ ), Prandtl number ( $Pr$ ), and Bingham number ( $Bn$ ), on the local and global momentum and heat transfer aspects. The results reported herein encompass the following ranges of conditions:  $1 \leq Re \leq 100$ ;  $1 \leq Pr \leq 100$ ;  $0 \leq Bn \leq 100$ . The value of aspect ratio ( $e$ ) was varied as 0.2, 0.5, 1, 2, and 5, thereby including both prolate and oblate shapes of spheroids. These results have been compared with the prior studies, both numerical and experimental, at least in the limit of Newtonian fluid behavior ( $Bn = 0$ ). The detailed structure of the flow field is studied in terms of the streamline patterns and yield surfaces separating the yielded and unyielded regions. The overall gross behavior is described in terms of drag coefficient and Nusselt number as functions of the above-noted parameters.

## 2. PROBLEM FORMULATION AND GOVERNING EQUATIONS

Consider the axisymmetric, steady, and incompressible flow of a Bingham plastic fluid with a free stream velocity,  $U_\infty$ , and temperature,  $T_\infty$ , over a heated spheroid of aspect ratio,  $e$ , whose surface is maintained at a constant temperature,  $T_w$ , as shown schematically in Figure 1. By simply changing the value of  $e$  and the axis of revolution, it is possible to vary the shape (prolate or oblate) and the aspect ratio of the spheroid, thereby providing a convenient method of delineating the effect of shape on the

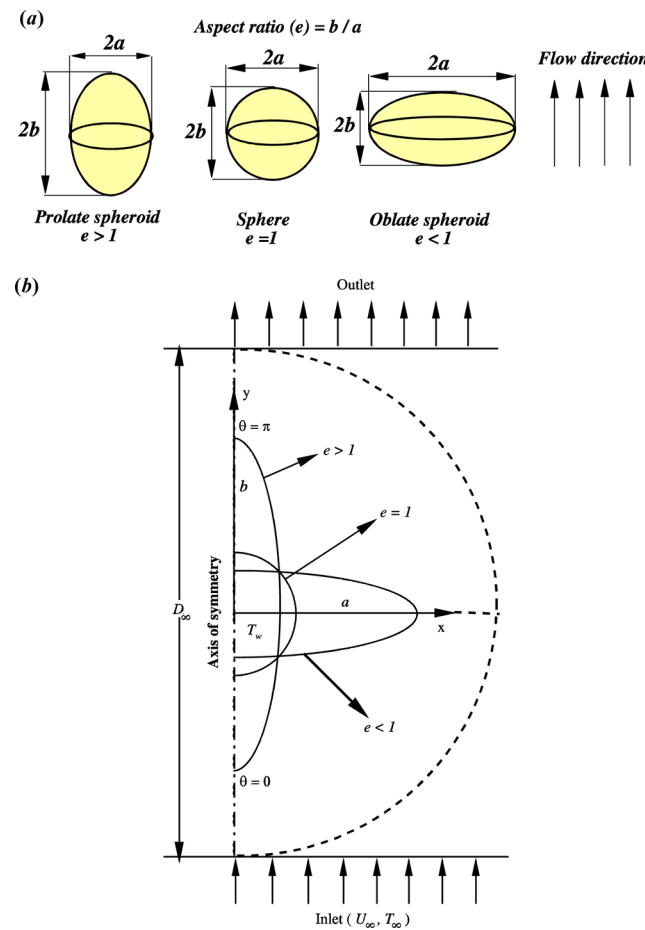


**Figure 1.** Schematics of the flow past a spheroid: (a) physical model; (b) computation domain.

momentum and heat transfer characteristics. Obviously, as it is not feasible to study numerically a truly unconfined flow, this approximation is reached here by enveloping the spheroid into an artificial concentric spherical shell of fluid of diameter,  $D_\infty$  (Figure 1b). A prudent choice of the value of  $D_\infty$  is necessary, as described in a later section. Due to the imposed temperature difference between the heated spheroid ( $T_w > T_\infty$ ) and the surrounding fluid, heat transfer occurs from the spheroid to the fluid. For the sake of simplicity, the thermo-physical properties appearing in the momentum and thermal energy equations (namely, specific heat,  $C$ , thermal conductivity,  $k$ , fluid density,  $\rho$ , Bingham yield stress,  $\tau_B$ , and plastic viscosity,  $\mu_B$ ) are all assumed to be independent of temperature and, similarly, the viscous dissipation effects in the energy equation are considered to be negligible (the maximum value of the Brinkman number ( $Br$ ) in this work is  $0.002 \ll 1$ , and hence, this assumption is justified here). Clearly, these two assumptions allow the momentum and energy equations to be solved in a sequential manner. Naturally, this simplification comes about at the expense of the fact that by necessity the maximum value of  $\Delta T (= T_w - T_\infty)$  present in the system must be small in order to neglect the temperature variation of the foregoing thermophysical properties. In this work, the maximum value of  $\Delta T$  used was 5 K, and it is therefore justified to evaluate the physical properties at the mean temperature of the fluid. Within the framework of the foregoing assumptions, the flow and temperature fields in the flow domain are given by

the mass, momentum, and thermal energy equations written in their dimensionless compact form as follows:

*Continuity equation:*

$$\nabla \cdot V = 0 \quad (1)$$

*Momentum equation:*

$$(V \cdot \nabla) V = -\nabla p + \frac{1}{Re} \nabla \cdot \tau \quad (2)$$

*Thermal energy equation:*

$$(V \cdot \nabla) \varphi = \frac{1}{Re \cdot Pr} \nabla^2 \varphi \quad (3)$$

For an incompressible fluid, the deviatoric part of the stress tensor ( $\tau$ ) is given as

$$\tau = 2\eta\dot{\gamma} \quad (4)$$

Here,  $\eta$  represents the scalar viscosity function and  $\dot{\gamma}$  is the rate of the deformation tensor, which can be written in terms of the velocity gradient tensor,  $\nabla V$ , and its transpose,  $\nabla V^T$ , as

$$\dot{\gamma} = \frac{1}{2}(\nabla V + \nabla V^T) \quad (5)$$

The magnitudes of the rate of deformation tensor and deviatoric stress tensor are given by

$$|\dot{\gamma}| = \sqrt{\frac{1}{2} II_{\dot{\gamma}}} \quad (6)$$

$$|\tau| = \sqrt{\frac{1}{2} II_{\tau}} \quad (7)$$

where

$$II_{\dot{\gamma}} = \text{tr}(\dot{\gamma}^2) \quad \text{and} \quad II_{\tau} = \text{tr}(\tau^2) \quad (8)$$

Here,  $II_{\dot{\gamma}}$  and  $II_{\tau}$  represent the second invariants of the rate of deformation tensor and the deviatoric stress tensor, respectively. For a Bingham fluid model, the deviatoric stress tensor can be expressed by

$$\tau = \left( 1 + \frac{Bn}{\sqrt{\frac{1}{2} II_{\dot{\gamma}}}} \right) \dot{\gamma}, \quad \text{if } II_{\tau} > 2Bn^2 \quad (9a)$$

$$\dot{\gamma} = 0, \quad \text{if } II_{\tau} \leq 2Bn^2 \quad (9b)$$

Due to the inherently discontinuous nature of the Bingham constitutive relation, eq 9, it is not suitable for a direct implementation in a numerical solution of the field equations. Currently several approaches<sup>39</sup> are available to circumvent this difficulty. However, two such approaches, which have gained wide acceptance and have been used extensively in the literature, are the so-called exponential regularization due to Papanastasiou<sup>40</sup> and the biviscous model.<sup>41</sup> While the merits and demerits of each of these and of the other such schemes have been discussed in detail by Glowinski and Wachs and others,<sup>39,42</sup> the Papanastasiou's regularization method is used here to obtain most of the results; limited results were, however, also obtained by using the biviscous model to contrast the performance of these two approaches. Using the

regularization method of Papanastasiou,<sup>40</sup> the Bingham constitutive relation is written as follows:

$$\tau = \left( 1 + \frac{Bn \left[ 1 - \exp \left( -m \sqrt{\frac{1}{2} II_{\dot{\gamma}}} \right) \right]}{\sqrt{\frac{1}{2} II_{\dot{\gamma}}}} \right) \dot{\gamma} \quad (10)$$

and thus, for a Bingham plastic fluid, the scalar viscosity function ( $\eta$ ) is given by the form:

$$\eta = \left( 1 + \frac{Bn \left[ 1 - \exp \left( -m \sqrt{\frac{1}{2} II_{\dot{\gamma}}} \right) \right]}{\sqrt{\frac{1}{2} II_{\dot{\gamma}}}} \right) \quad (11)$$

In eqs 10 and 11,  $m$  is the dimensionless regularization parameter, which controls the exponential growth of the stress, thereby converting the abrupt transition from the solid-like to fluid-like behavior into a gradual one. Of course, in the limit of  $m \rightarrow \infty$ , eq 10 coincides with eq 9 and  $m \rightarrow 0$  corresponds to the Newtonian fluid behavior. Similarly, the biviscous model approach relies on replacing the solid-like regime by an equivalent fluid of extremely high viscosity (the so-called yielding viscosity,  $\mu_y$ ) written as follows:

$$\tau = \left( \frac{\mu_y}{\mu_B} \right) \dot{\gamma} \quad \text{for } II_{\tau} \leq 2Bn^2 \quad (12)$$

$$\tau = Bn + \left( \dot{\gamma} - \frac{Bn}{\mu_y/\mu_B} \right) \quad \text{for } II_{\tau} > 2Bn^2 \quad (13)$$

In this case, the true Bingham behavior is obtained in the limit of  $\mu_y \rightarrow \infty$ . Thus, in both cases, one must use large values of  $m$  or  $\mu_y/\mu_B$  to obviate the discontinuous nature of the constitutive relationship.

The problem definition and formulation is completed by identifying the physically realistic boundary conditions. On the surface of the spheroid, the standard no-slip condition and that of constant temperature ( $\varphi = 1$ ) are used. The lower half of the artificial spherical domain is treated as inlet (Figure 1b), and here the uniform velocity in the  $y$ -direction ( $V_y = 1$ ) and constant temperature ( $\varphi = 0$ ) are prescribed on this surface. Similarly, the upper half of the surrounding envelope of fluid is designated as the outlet (Figure 1b) and the zero-diffusion flux of all primitive variables (except pressure) is employed here, i.e.,  $(\partial \phi / \partial y) = 0$ , where  $\phi = V_x, V_y$  or  $\varphi$ . Over the range of conditions spanned here, the flow is considered to be axisymmetric, and therefore, the numerical solution is sought only in the half flow domain to economize on the required computational effort, similar to the case of a sphere.<sup>13,14</sup>

The aforementioned governing and constitutive equations and the boundary conditions are rendered dimensionless by using  $2a$ ,  $U_\infty$ ,  $\rho U_\infty^2$ ,  $(2a/U_\infty)$ , and  $(\mu_B U_\infty / 2a)$  as the scaling variables for length, velocity, pressure, time, and stress components, respectively. Also, the temperature is made dimensionless as  $\varphi = (T - T_\infty) / (T_w - T_\infty)$ . Thus, the scaling considerations suggest that the velocity and temperature fields in this case are governed by four dimensionless numbers, namely, Reynolds number,  $Re$ , Bingham number,  $Bn$ , Prandtl number,  $Pr$ , and, of course, the aspect ratio,  $e$ , of the spheroid. For a Bingham plastic fluid, these are defined as follows:

**Reynolds number:**

$$Re = \frac{U_\infty \rho (2a)}{\mu_B} \quad (14)$$

**Bingham number:**

$$Bn = \frac{\tau_o (2a)}{\mu_B U_\infty} \quad (15)$$

The two limits,  $Bn \rightarrow 0$  and  $Bn \rightarrow \infty$  correspond to the Newtonian fluid behavior and the fully plastic flow region, respectively.

**Prandtl number:**

$$Pr = \frac{\mu_B C}{k} \quad (16)$$

Finally, of course, the aspect ratio of the spheroid  $e = (b/a)$  is also a dimensionless parameter which describes the shape of the spheroidal particle.

At this juncture, it is worthwhile to note here that the preceding definitions are based on the choice of the constant Bingham plastic value as the viscosity scale, and naturally, this choice does not incorporate the effect of fluid yield-stress. Alternatively, one can use the effective fluid viscosity given by  $(\mu_B + \tau_o/|\dot{\gamma}_c|)$ , where, in turn, the characteristic shear rate is considered to be of the order  $\dot{\gamma}_c \sim (U_\infty/2a)$ . This choice of viscosity scale leads to the following modified definitions of the Reynolds and Prandtl numbers:

$$Re^* = \frac{Re}{1 + Bn}; \quad Pr^* = Pr(1 + Bn) \quad (17)$$

Finally, the numerical solution of the preceding dimensionless governing equations together with the boundary conditions maps the flow domain in terms of the velocity, pressure, and temperature fields ( $u - v - p - \varphi$ ) as functions of the four influencing parameters, namely,  $Re$ ,  $Pr$ ,  $Bn$ , and  $e$ . These results, in turn, can be postprocessed to visualize the spatial variation of the flow and temperature fields in terms of the streamline and isotherm contours in the close proximity of the spheroid to delineate the wake regions, local hot/cold spots, etc. Also, the size and locations of yielded/unyielded regions in the flow domain are important in viscoplastic fluids, as they provide useful insights about the extent of local deformation and mixing of fluids. Next, the gross fluid mechanical and heat transfer aspects are analyzed in terms of the variation of the local Nusselt number along the spheroid surface. Finally, the overall features are characterized in terms of the drag coefficient and average Nusselt number as functions of the four pertinent dimensionless groups, i.e.,  $Re$ ,  $Bn$ ,  $e$ , and  $Pr$ . Since detailed descriptions of such postprocessing are available elsewhere,<sup>13,14</sup> only their definitions are presented here.

$$C_{DP} = \frac{F_{DP}}{\frac{1}{2}\rho U_\infty^2 A_p} \quad (18)$$

$$C_D = \frac{F_D}{\frac{1}{2}\rho U_\infty^2 A_p} \quad (19)$$

$$Nu_\theta = \frac{h(2a)}{k} = -\frac{\partial \varphi}{\partial n_s} \quad (20)$$

and

$$Nu_{avg} = \frac{1}{S} \int_0^S Nu_\theta dS \quad (21)$$

Dimensional analysis shows the drag coefficient to be a function of the Reynolds number, Bingham number, and aspect ratio of the spheroid whereas the Nusselt number shows additional dependence on the Prandtl number. The present study endeavors to develop an understanding of this functional relationship. Before leaving this section, it is readily acknowledged that the COMSOL solver used here solves the field equations in their dimensional form, but writing these equations in their suitable dimensionless forms, such as eqs 1–13, here elucidates the relative importance of the various terms in the momentum and energy equations.

### 3. SOLUTION METHODOLOGY AND CHOICE OF COMPUTATIONAL PARAMETERS

Since detailed descriptions of the overall numerical solution methodology used here are available in our recent studies,<sup>13,14,22,23</sup> only the salient aspects are described here briefly. In brief, the finite element method based solver COMSOL Multiphysics (version 4.2a) was used both for the meshing purpose and for mapping the flow domain in terms of the primitive variables. The axisymmetric, steady, laminar, and single fluid module along with the parallel direct linear solver (PARDISO) was used. The quadrilateral elements were used with nonuniform spacing in the whole computational domain. Due to the no-slip and constant temperature boundary conditions imposed on the surface of the spheroid, very fine quadrilateral cells have been used in the vicinity of the spheroid to resolve the steep velocity and temperature gradients in this region. Similarly, a fine grid was also used at the interface of the yielded/unyielded regions to delineate the yield surfaces as accurately as possible. A relative convergence criterion of  $10^{-6}$  was used for both the velocity and temperature fields. Within this framework, the drag and Nusselt number values had also stabilized at least up to four significant digits. The results obtained using more stringent convergence criteria altered the values negligibly. A user defined function (UDF) was used to implement the modified Bingham model with the Papanastasiou exponential regularization to approximate the deviatoric stress tensor in the momentum equation. As noted earlier, most such solvers employ the dimensional form of the momentum and energy equations. However, in order to enhance the practical utility and appeal of the resulting numerical values, it is customary to report and correlate such results in their appropriate dimensionless form, and hence, the equations are presented here in their nondimensional form. Therefore, to achieve the desired values of the dimensionless parameters such as  $Bn$ ,  $Pr$ ,  $Re$ , and  $e$ , appropriate values of the fluid properties (i.e.,  $k$ ,  $\mu_B$ ,  $\rho$ ,  $\tau_o$ , and  $C$ ) and geometrical parameters ( $a$  and  $b$ ) were specified. These specific values are, however, of no particular significance because the final results are presented in terms of the relevant dimensionless parameters only. Finally, the yield surfaces (boundary between the yielded-and unyielded-region) were delineated by comparing the local stress level with the yield stress of the fluid using the tolerance limit of  $10^{-6}$ – $10^{-7}$  within the framework of the von Mises

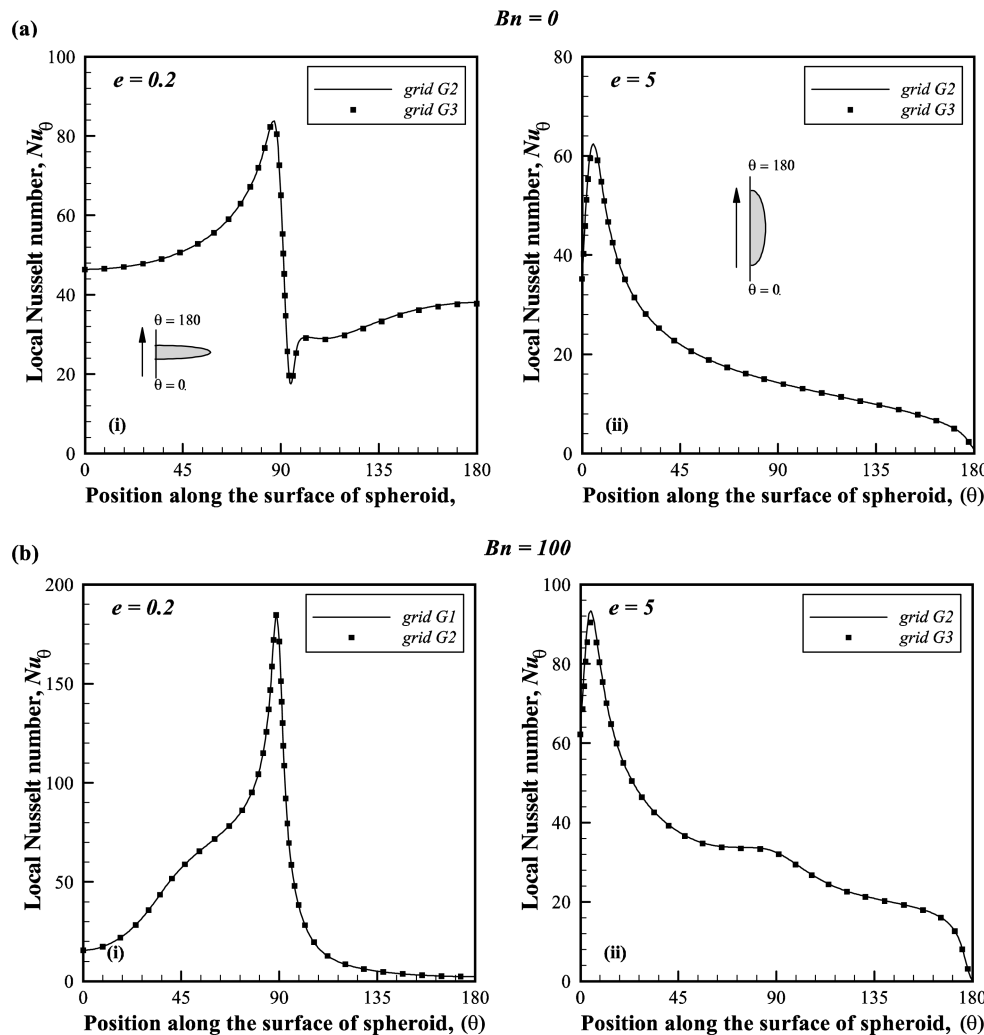


**Figure 2.** Effect of grid resolution on the local Nusselt number variation along the surface of the spheroid at  $Re = 100$  and  $Pr = 100$ : (a)  $Bn = 0$ ; (b)  $Bn = 100$ .

yielding criterion. This value was arrived at by initial exploratory studies.

The importance of a prudent choice of  $D_\infty$ , computational mesh, and value of  $m$  or  $\mu_y$  need not be overemphasized here for the present results to be free from numerical artifacts. Following the strategy employed in our recent studies,<sup>13,14,22,23</sup> the value of  $(D_\infty/2b)$  was systematically varied between 10 and 300 depending upon the values of the aspect ratio ( $e = 0.2, 1$ , and  $5$ ) for the lowest values of the Reynolds number ( $Re = 1$ ) and the Prandtl number ( $Pr = 1$ ) and the extreme values of the Bingham number (i.e.,  $Bn = 0$  and  $100$ ), as the velocity and temperature fields are known to exhibit slow spatial decay under these conditions. Thus, the value of  $(D_\infty/2b)$  found to be suitable under such extreme conditions is likely to be satisfactory over the range of conditions encompassed here. Tables S1(a), S1(b), and S1(c) of the Supporting Information summarize the results showing the effect of  $(D_\infty/2b)$  on the values of the drag and Nusselt number. Considering the small changes in the results (<0.5%), the values of  $(D_\infty/2b) = 140$ ,  $100$ , and  $40$  (these values can readily be re-expressed in terms of  $2a$ ) for  $e = 0.2, 1$ , and  $5$ , respectively, are regarded to be satisfactory and acceptable for the present results to be free from boundary effects. Next, similarly, three numerical meshes (detailed in Table S2) comprising varying numbers of elements

on the surface of the spheroid ( $N_p$ ) as well as in the domain (based on half-domain) were created for selecting an optimal grid in the present study. Since the boundary layer thickness is expected to be minimum at the maximum values of the Reynolds, Prandtl, and Bingham numbers, grid effects have been investigated at  $Re = 100$ ,  $Pr = 100$ , and at the two extreme values of the Bingham number, i.e.,  $Bn = 0$  and  $Bn = 100$  used here. An examination of the results reported in Table S2 suggests that grid G2 is sufficiently fine to resolve the steep gradients in the thin boundary layers under such extreme conditions; albeit, the domain effects seem to be most prominent for the limiting case of the Newtonian fluids due to the slow spatial decay of the velocity. Conversely, due to the finite size of the fluid-like regions, it is possible to use shorter computational (and also in such experiments) domains to minimize the boundary effects in the case of viscoplastic fluids. This choice is further justified here by examining the effect of the grid on the distribution of the surface pressure and the local Nusselt number along the surface of the heated spheroid in Newtonian fluids, as shown in Figure 2. Indeed, the predictions of grids G2 and G3 are virtually indistinguishable from each other. Thus, on either count, grid G2 in each case is regarded to be satisfactory.

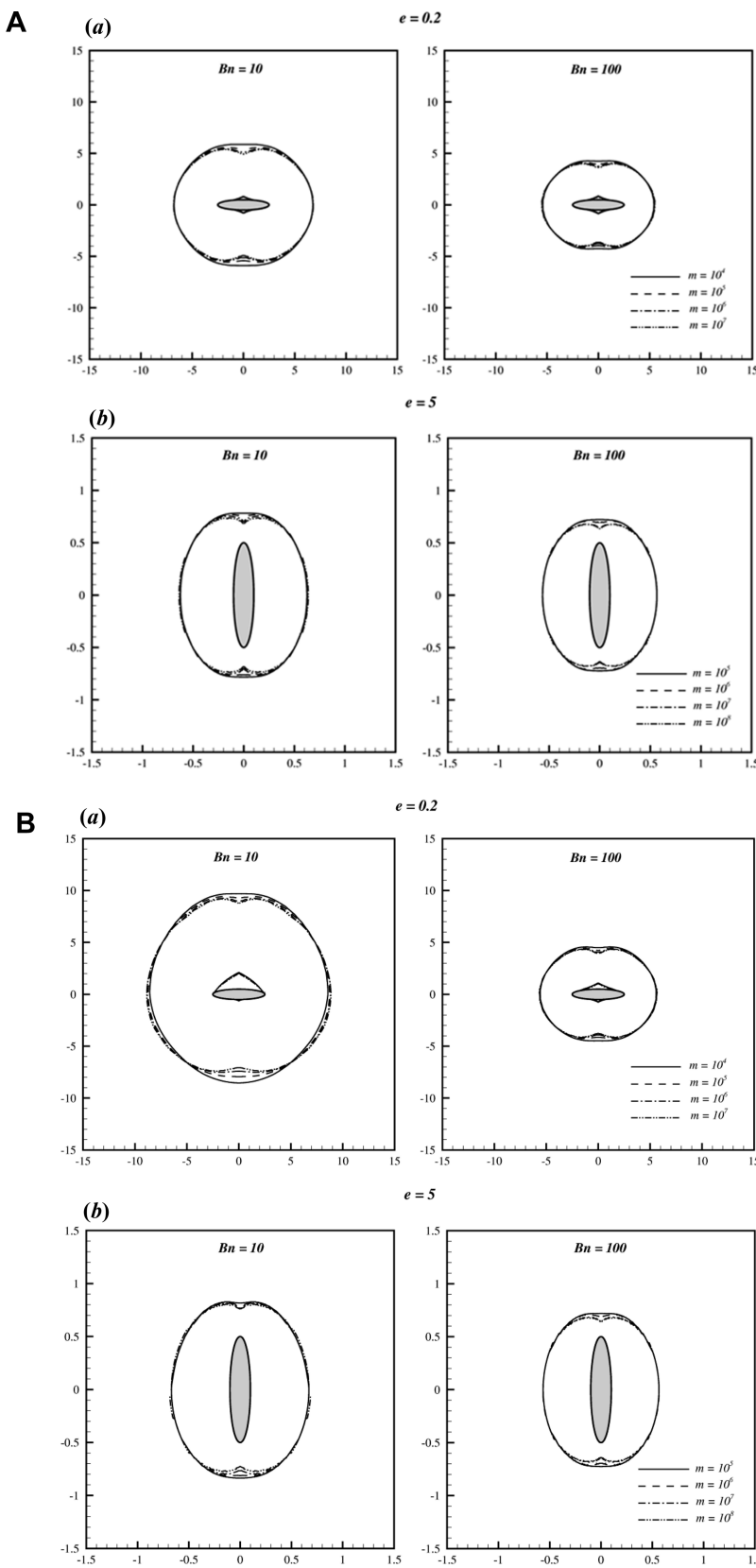


**Figure 3.** Influence of growth rate parameter ( $m$ ) on the position of yielded/unyielded regions at (A)  $Re = 1$  and (B)  $Re = 100$ : (a)  $e = 0.2$ ; (b)  $e = 5$ .

Finally, the regularized Bingham fluid model also contains an adjustable parameter, namely  $m$  or  $\mu_y$ , depending upon the scheme used. Naturally, one must use as large a value of  $m$  (or  $\mu_y$ ) as possible to capture the true Bingham fluid behavior.

However, excessively large values of  $m$  make the coefficient matrix very stiff, which can lead to numerical instabilities in the solution in terms of oscillations and/or poor convergence characteristics. Therefore, there is a trade-off between the

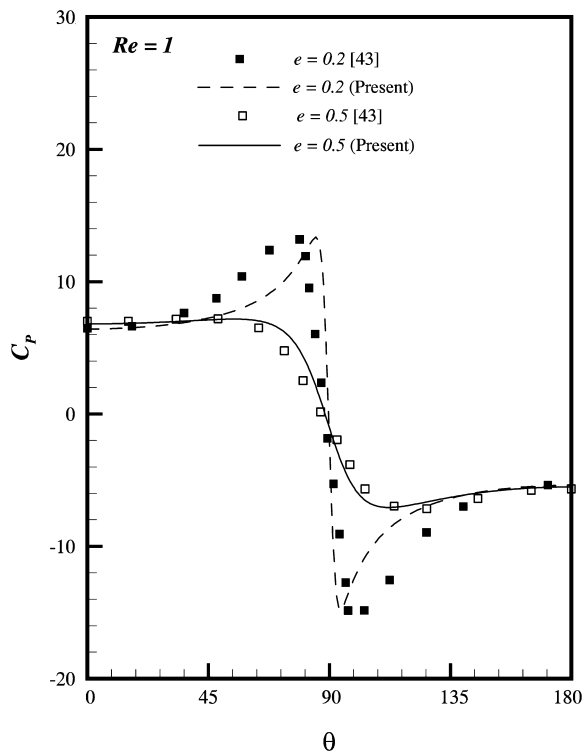


**Figure 4.** Distribution of pressure coefficient in dimensionless form ( $C_p$ ) along the spheroid surface.

**Table 1.** Comparison of the Present Drag Coefficient Values with That of Ref 44 in Newtonian Fluids ( $Bn = 0$ )

Re	$C_D$			
	$e = 0.9$		$e = 1.11$	
	ref 44	Present	ref 44	Present
10	3.97	3.93	4.56	4.74
20	2.42	2.51	2.87	2.96
30	1.91	1.97	2.26	2.29
40	1.63	1.67	1.93	1.93
50	1.46	1.48	1.72	1.69
60	1.33	1.34	1.56	1.52
70	1.23	1.25	1.45	1.40
80	1.16	1.16	1.35	1.30
90	1.12	1.09	1.28	1.22
100	1.04	1.03	1.22	1.15

precision of the results on one hand and the numerical issues on the other. Bearing in mind this aspect, Table S3 and parts A and B of Figure 3 summarize the results, for the two extreme values of the Reynolds number  $Re = 1$  and 100, showing the influence of  $m$  on the numerical values. Evidently,  $m = 10^6$  for  $e \leq 1$  and  $m = 10^7$  for  $e > 1$  are found to be sufficient over the range of conditions spanned here. The selection of these values is further justified by presenting a series of benchmark comparisons in the next section.

#### 4. RESULTS AND DISCUSSION

In this study, the governing differential equations have been solved numerically to delineate the effects of the Reynolds number, Prandtl number, Bingham number, and aspect ratio on the momentum and heat transfer from a spheroid over the following ranges of dimensionless parameters:  $1 \leq Re \leq 100$ ,  $1 \leq Pr \leq 100$ ,  $0 \leq Bn \leq 100$ , and  $0.2 \leq e \leq 5$ . A comment regarding

**Table 2.** Comparison of the Present Friction Drag Coefficient Values for Spheroids with That of Ref 28 in Newtonian Fluids ( $Bn = 0$ )

Re	$C_{DF}$	
	ref 28	Present
$e = 0.5$		
1	23.620	23.467
10	3.6108	3.5899
20	2.2163	2.2023
50	1.1850	1.1727
100	0.7197	0.7130
$e = 1$		
1	18.309	18.345
10	2.7990	2.8015
20	1.7180	1.7123
50	0.9284	0.9211
100	0.5821	0.5805
$e = 2$		
1	13.748	13.836
10	2.1242	2.1089
20	1.290	1.2792
50	0.6898	0.6847
100	0.4417	0.4357

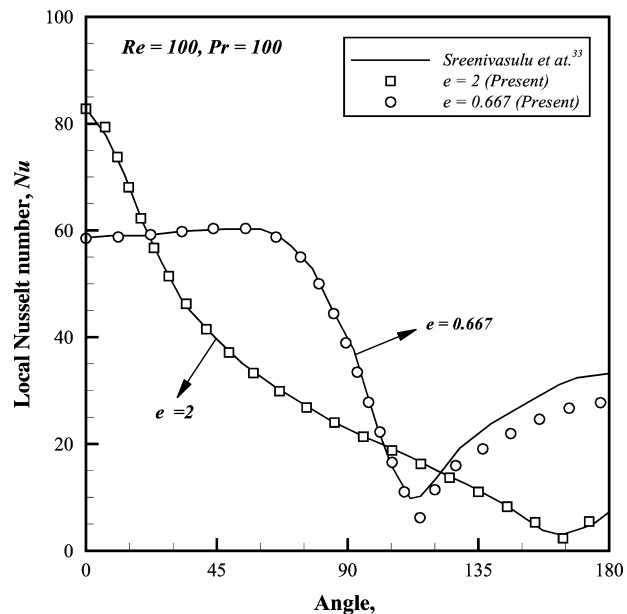


**Figure 5.** Comparison of the present local Nusselt number variation over the surface of a spheroid with that of ref 33 at  $Re = 100$  and  $Pr = 100$  for Newtonian fluids.

the choice of the ranges of these parameters is in order. The available studies for the flow of Newtonian fluids past oblates and prolates, e.g., see refs 43 and 44, confirm the flow regime to be steady and axisymmetric at least up to  $Re = 100$ . While no analogous study is available for Bingham plastic fluids, the fluid yield stress tends to stabilize the flow, and therefore, this assumption is reasonable under the present circumstances. Similarly, most such fluids exhibit the value of the Prandtl number as high as 100 or even higher; e.g., see refs 4–8. However, it is readily recognized that ultrafine numerical meshes are needed to resolve increasingly thin boundary layers with increasing Prandtl numbers. On the other hand, a hundred-fold variation in the value of the Prandtl number spanned here is considered

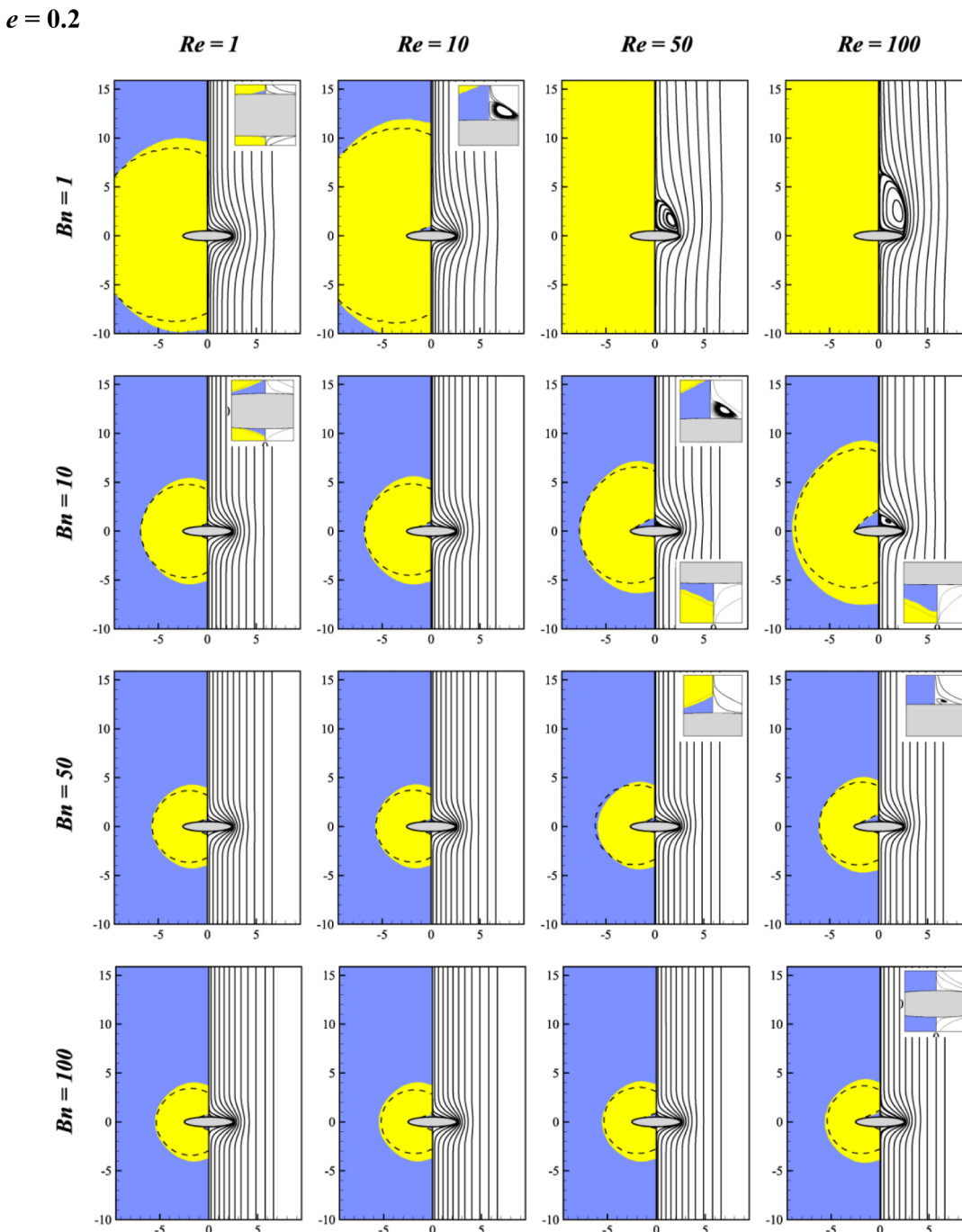


**Figure 6.** Morphology of the yield surfaces (left half) and corresponding streamlines (right half) for  $e = 0.2$  (dashed lines represent biviscosity model at  $\mu_y/\mu_B \geq 10^4$ ).

to be adequate to delineate the scaling of the Nusselt number on the Prandtl number. The minimum value of the Bingham number,  $Bn = 0$ , corresponds to the Newtonian fluid behavior. With the increasing values of the Bingham number, the yielded regions diminish in size, thereby sharpening the gradients in these regions, eventually approaching the fully plastic flow limit. Thus, our interest lies mainly in the intermediate regime of the Bingham number. In summary, the ranges of the relevant parameters selected here are thus dictated by a combination of practical and numerical considerations. However, before undertaking a detailed presentation and discussion of the new results, it is instructive to establish the reliability and precision of the numerical solution methodology and computational

parameters selected here. This objective is accomplished here by presenting a few benchmark comparisons in the next section.

**4.1. Validation of Results.** While extensive validation for the flow and heat transfer in Bingham plastic fluids from a sphere<sup>13,14</sup> or circular<sup>22</sup> and elliptical<sup>23</sup> cylinders has been reported elsewhere, only the additional comparisons for spheroidal particles are included here. For Newtonian fluids, the present results ( $Bn = 0$ ) have been compared with the prior experimental data<sup>30</sup> and numerical studies<sup>31,43</sup> for three values of  $e = 0.2, 2$ , and  $5$ . The present values are found to be within  $\pm 5\%$  of ref 30 and  $\pm 6\%$  of refs 31 and 43. Furthermore, the present values of the dimensionless pressure at the front stagnation point for a spheroid ( $e = 0.2$ ) are also observed to be

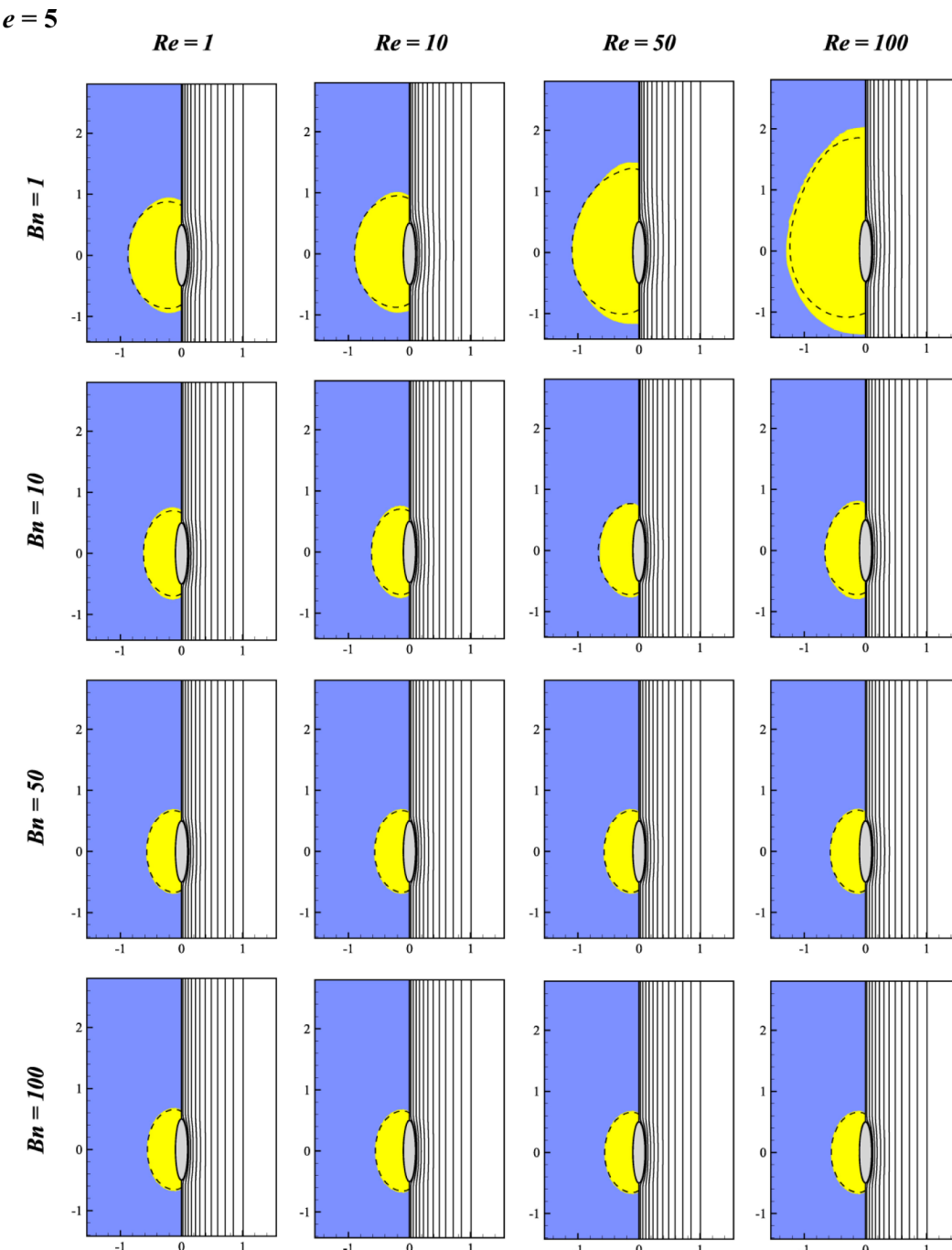


**Figure 7.** Morphology of the yield surfaces (left half) and corresponding streamlines (right half) for  $e = 5$  (dashed lines represent biviscosity model at  $\mu_y/\mu_B \geq 10^4$ ).

within  $\pm 2.5\%$  of the literature values,<sup>43</sup> whereas the corresponding surface pressure distribution is shown in Figure 4; the agreement is seen to be satisfactory, bearing in mind that the computational mesh used in ref 43 is rather coarse as compared to the one used here. Tables 1 and 2 compare the drag predictions with some of the recent studies,<sup>28,44</sup> and once again the three predictions based on different numerics and domain, etc., show excellent ( $\sim 2.5\%$ ) correspondence with each other. Next, Figure 5 shows a comparison in terms of the local Nusselt number with that of Sreenivasulu et al.,<sup>33</sup> and once again, the match is seen to be very good. Suffice it to add here that the present average Nusselt number values are within  $\pm 1.5\%$  of that reported in ref 33. In addition, a comparison between the

present average Nusselt number values and that of refs 13 and 35 for a sphere ( $e = 1$ ) is presented in Table S4 and the present numerical results were seen to be within  $\pm 4\%$ . Finally, the present values of the recirculation lengths in Newtonian fluids were found to be within 2–2.5% of that reported in ref 44 for spheroidal particles.

One possible explanation for the minor discrepancies seen in the foregoing comparisons is the fact that, in most previous studies, a single value of  $(D_\infty/2b)$  and numerical mesh have been used for all values of  $e$  whereas, in the present work, both the domain size and numerical mesh were customized for each value of  $e$ , and therefore, the present results are regarded to be more reliable on this count as well. In summary, the new results

**Table 3. Comparison between the Papanastasiou and Biviscosity Models in Terms of Total Drag Coefficient Values at  $Bn = 100$  and  $\mu_y/\mu_B = 10^4$**

$Re$	Papanastasiou model	Biviscosity model
$e = 0.2$		
1	2661.1	2660.8
5	532.24	531.82
10	266.16	265.91
50	53.482	53.440
100	27.067	27.043
$e = 1$		
1	3207.1	3207.1
5	641.43	641.16
10	320.44	320.73
50	64.171	64.198
100	32.197	32.220
$e = 5$		
1	6718.0	6718.0
5	1343.6	1343.3
10	671.80	671.80
50	134.37	134.34
100	67.194	67.194

reported herein for spheroids in Bingham plastic fluids are considered to be reliable to within  $\pm 2\%$  or so.

**4.2. Structure of Yielded/Unyielded Regions.** The simultaneous existence of the yielded and unyielded zones is a distinct and unique feature of the Bingham plastic fluids. Figures 6 and 7 show the representative results elucidating the effect of the Reynolds number, Bingham number, and aspect ratio on the yield surfaces separating the yielded and unyielded parts of the fluid. Owing to the symmetry, the yielded surfaces are shown only in the left half of the domain in these figures. In the present case, two distinct unyielded zones are observed, as can be seen in Figure 6 (for  $e = 0.2$ ) and Figure 7 (for  $e = 5$ ), where unshaded parts represent the fluid-like or yielded zones. Broadly, velocity gradients (and hence the stress levels) are very steep in the regions close to the surface of the spheroids due to the imposition of the no-slip condition. As the level of the shearing gradually drops away from the spheroid, the stress level drops in accordance with the regularized Bingham model, whereby a point is reached when the magnitude of the stress falls below the fluid yield stress, thereby leading to the formation of the unyielded zone moving *en masse* with the uniform translational velocity, as can be seen in these figures. Furthermore, at large values of the Reynolds number, two triangular

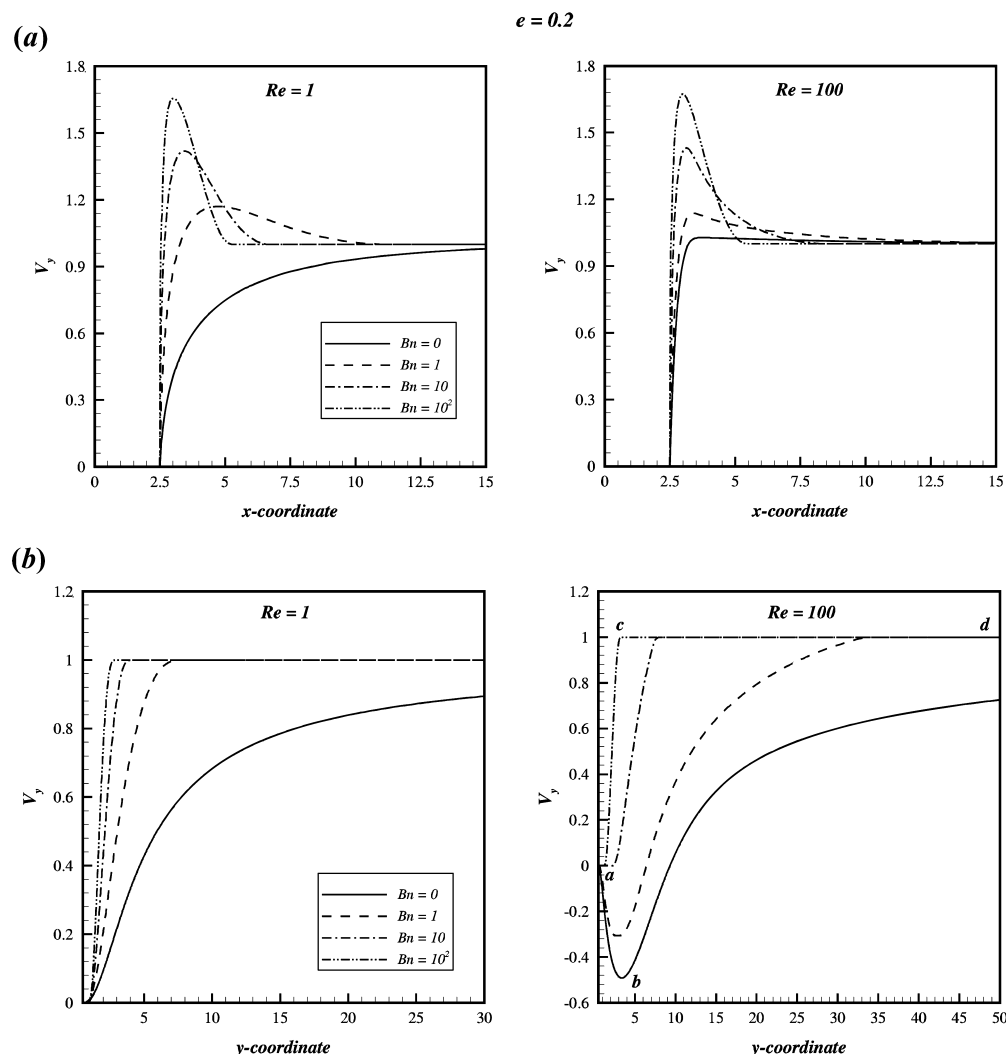


**Figure 8.** Axial velocity profile for  $e = 0.2$  at  $Re = 1$  and  $100$ : (a) along line  $y = 0$  and  $x > 0$ ; (b) along line  $x = 0$  and  $y > 0$ .

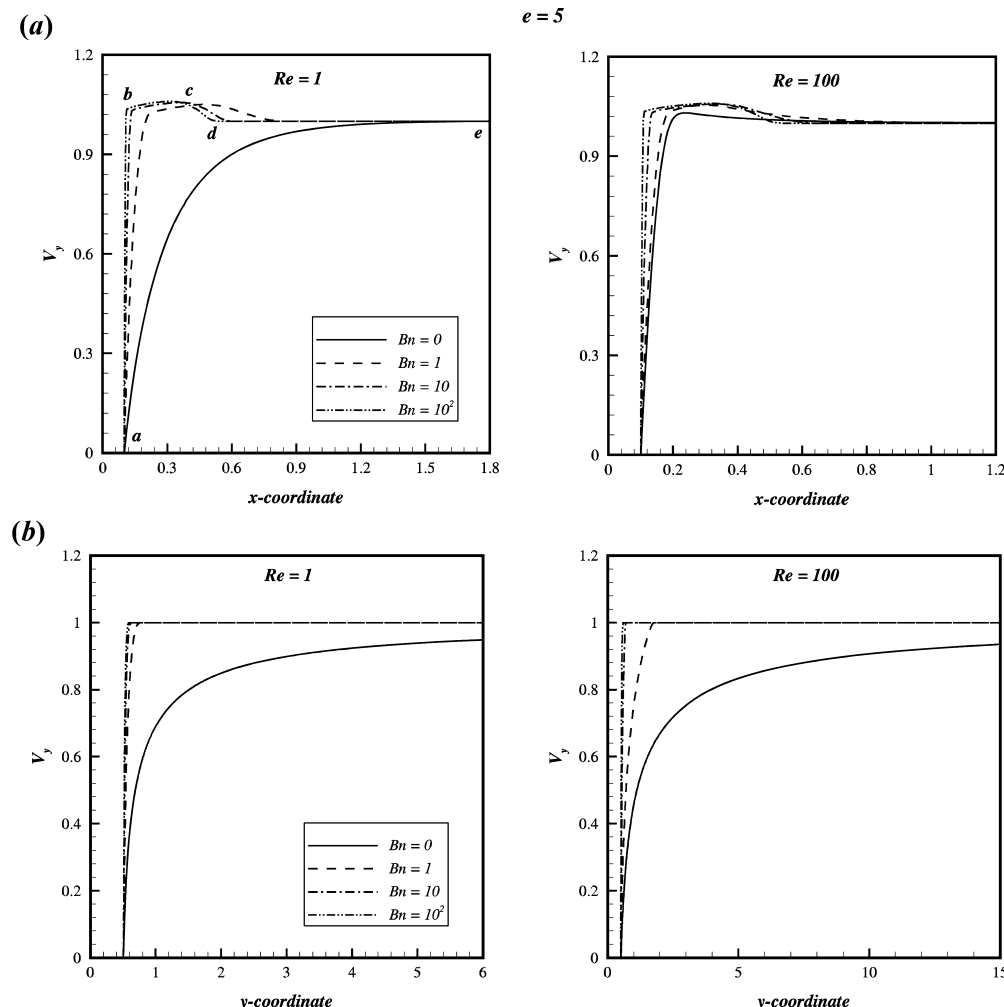


**Figure 9.** Axial velocity profile for  $e = 5$  at  $Re = 1$  and 100: (a) along line  $y = 0$  and  $x > 0$ ; (b) along line  $x = 0$  and  $y > 0$ .

shaped unyielded zones (polar caps) can also be discerned near the front and rear stagnation points which, however, are static in nature. Notwithstanding the finite values of the Reynolds number in the present case, these regions are qualitatively similar to that obtained by Beris et al.<sup>10</sup> for the creeping flow past a sphere and by Nirmalkar et al.<sup>13,14</sup> at finite Reynolds numbers. Since the delineation of the boundaries separating the yielded and unyielded parts of the flow domain is of great significance, additional simulations were also performed using the biviscous model by using the values of the yielding viscosity in the range ( $10^4 \leq (\mu_y/\mu_B) \leq 10^7$ ) to corroborate the predictions of the Papanastasiou model. These predictions of the yield surfaces are also shown in Figures 6 and 7 as broken lines. An excellent agreement is seen to exist between the two results, thereby lending credibility to the reliability of the present results. The comparison between these two approaches is also shown in terms of total drag coefficient values, and the results are within  $\pm 0.1\%$  of each other (Table 3). Hence, either of these two approaches can be used with appropriate values of  $m$  or  $(\mu_y/\mu_B)$  in a new situation. Clearly, the size of the yielded and/or unyielded segments depends on the flow parameters,  $Re$  and  $Bn$ , and on the aspect ratio of the spheroid. In overall terms, irrespective of the value of the aspect ratio, the fluid-like (yielded) regions grow in size with the increasing value of the Reynolds number due to the increasing inertial effects. This tendency is countered by the increasing Bingham number.

Also, as the spheroid becomes increasingly blunt, the size of the rear triangular static zone increases; while these zones progressively diminish as the degree of streamlining increases, i.e., as one passes from an oblate to a prolate shape. All else being equal, one can anticipate from the present results that, for an oblate ( $e < 1$ ), shearing in the fluid extends farther than that for a prolate ( $e > 1$ ); this corresponds to the fact that the extent of yielded substance progressively shortens while moving toward the prolate geometry. Furthermore, increasing values of the Bingham number suppress the flow field; thereby, the far away yield surface moves closer to the solid object. For a given Reynolds number and particle shape, there exists a limiting Bingham number beyond which the flow conditions correspond to the limit of the fully plastic flow. Conversely, at high values of the Bingham number, inertia in the fluid is completely overshadowed by the increased yield stress effects, and therefore, no significant changes in the flow field are expected with the increasing values of the Reynolds number beyond this critical value. Overall, the size of the fluid-like yielded regions is thus influenced by the values of the Reynolds number, Bingham number, and aspect ratio of the spheroid.

**4.3. Streamline Patterns.** It is customary to visualize the spatial variation of the flow field in terms of the streamline contours; as such plots delineate the regions of accelerating/decelerating flow and stagnant and also circulating or wake regions in the flow domain. Thus, representative streamline

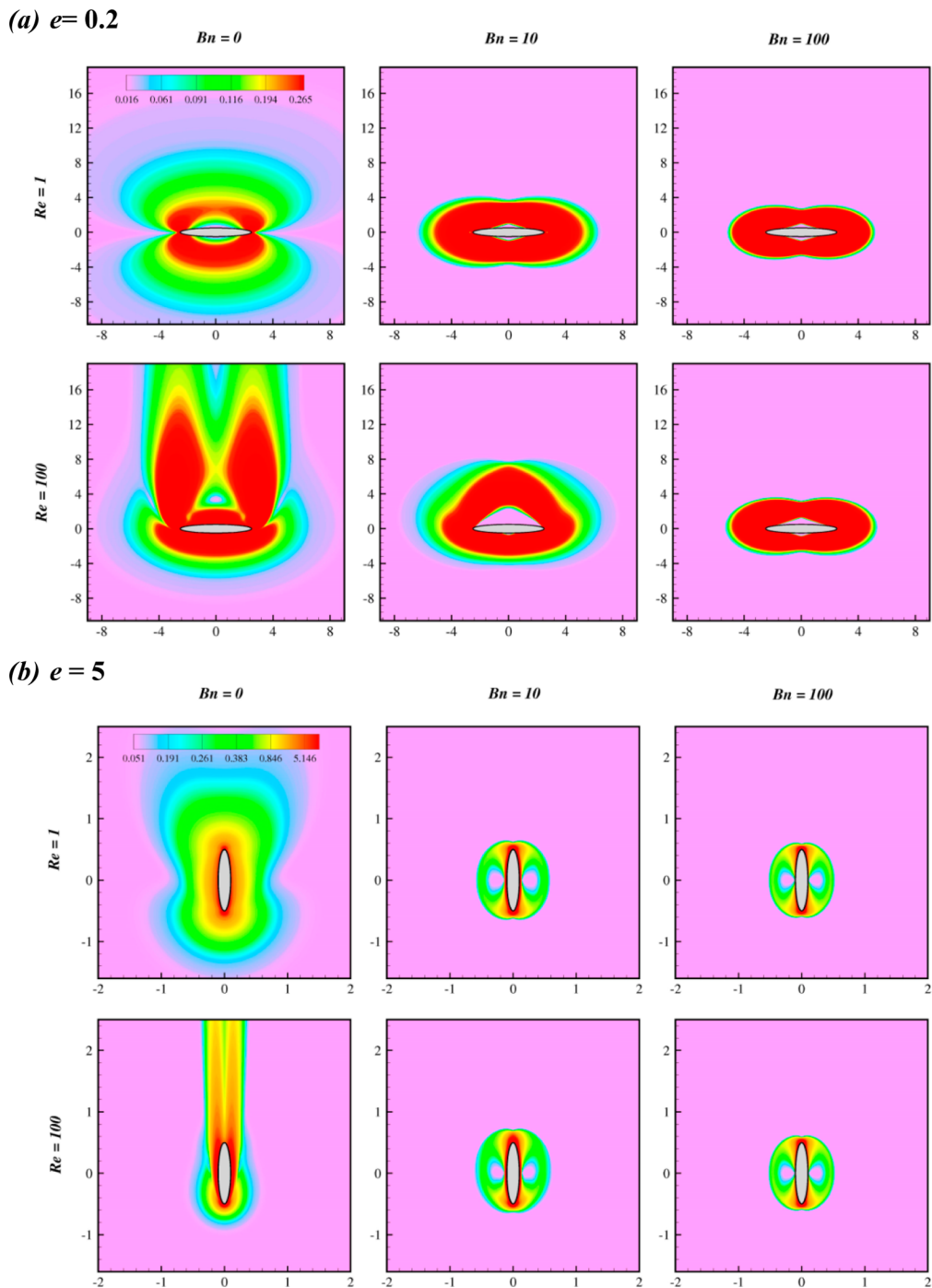


**Figure 10.** Effect of the Reynolds number ( $Re$ ) and Bingham number ( $Bn$ ) on shear rate contours near the spheroid surface: (a)  $e = 0.2$ ; (b)  $e = 5$ .

profiles are shown for scores of values of the Reynolds number and Bingham number and for two values of the aspect ratios ( $e = 0.2$  and 5) in Figures 6 and 7 on the right half of each figure. At low values of the Reynolds number, due to negligible inertia, a fluid element is able to negotiate the surface contour of the spheroid; therefore, the flow remains attached to the surface of the spheroid irrespective of the value of the aspect ratio under such conditions. As the value of the Reynolds number is gradually incremented, the fluid inertia increases, and this can lead to the establishment of the adverse pressure gradient in the rear part of the spheroid and eventually lead to flow separation and hence the formation of the recirculation region. Strictly speaking, the latter is characterized by a single

torus-shaped region which in a cut plane appears in the form of two counter-rotating symmetric vortices in the rear side of the spheroid. Therefore, it needs to be emphasized here that, in spite of their appearance, the present 3-D results should not be confused with the 2-D planar flow, such as that over a circular cylinder. For a given shape, the length of the wake increases in the axial direction with the increasing Reynolds number and it also broadens as the point of separation moves upstream along the surface of the spheroid. Similarly, with the blunting of the body shape or decreasing the value of  $e$  (sudden diverging area), the flow separation occurs at lower and lower Reynolds numbers, as can be seen in Figure 6. This tendency, however, is seen to be suppressed with the introduction of fluid yield stress

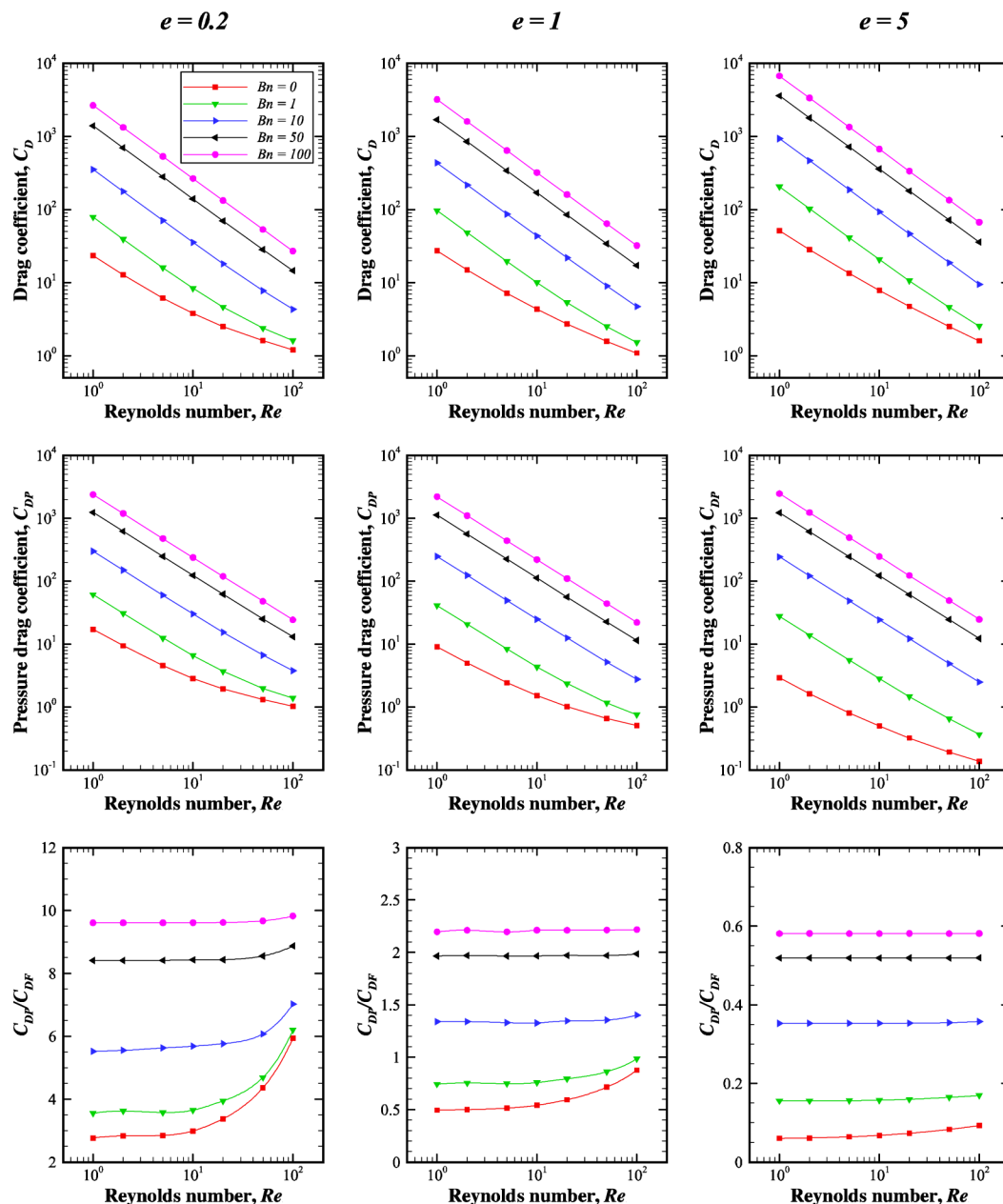


**Figure 11.** Dependence of total drag coefficient ( $C_D$ ), pressure drag coefficient ( $C_{DP}$ ), and ratio of pressure drag coefficient to friction drag coefficient ( $C_{DP}/C_{DF}$ ) on the Reynolds number, Prandtl number, and Bingham number.

**Table 4. Constants of Eq 23 with the Corresponding Errors**

$e$	$b_0$	$c_0$	% Error	
			Mean	Max.
0.2	0.34	0.26	11.8	41.6
0.5	0.42	0.19	12.0	39.6
1	0.60	0.13	12.2	36.7
2	1.04	0.09	12.1	30.8
5	2.40	0.06	11.9	22.9

(i.e.,  $Bn$ ). This trend can clearly be seen in Figure 6 when one goes down along a column. Thus, it is possible to prevent the flow separation in such fluids even at  $Re = 100$  for a sphere (not shown here for the sake of brevity) by introducing as small a value of  $Bn$  as  $Bn = 1$ . One can explain this behavior by considering the presence of the unyielded material encapsulat-

ing the spheroid, and the confining walls are known to suppress the phenomenon of flow separation. It is thus possible to manipulate the nature of the flow field by altering the rheological properties of the carrier medium, as is practiced in the thermal treatment of foodstuffs. However, a word of caution is in order here. Even though the so-called unyielded material attached to the spheroid should strictly speaking be stagnant, but it is not so, as can be seen in the form of a small recirculation region in the case of  $Bn = 10$  and  $Re = 50$  (and possibly for other combinations too) in Figure 6. This ambiguous behavior is a direct consequence of the regularization approximation used in such computations, all of which replace the unyielded solid-like subregions by a highly viscous fluid. Needless to say, the corresponding values of the stream function in such regions are several orders of magnitude lower than that in the fluid-like yielded regions.

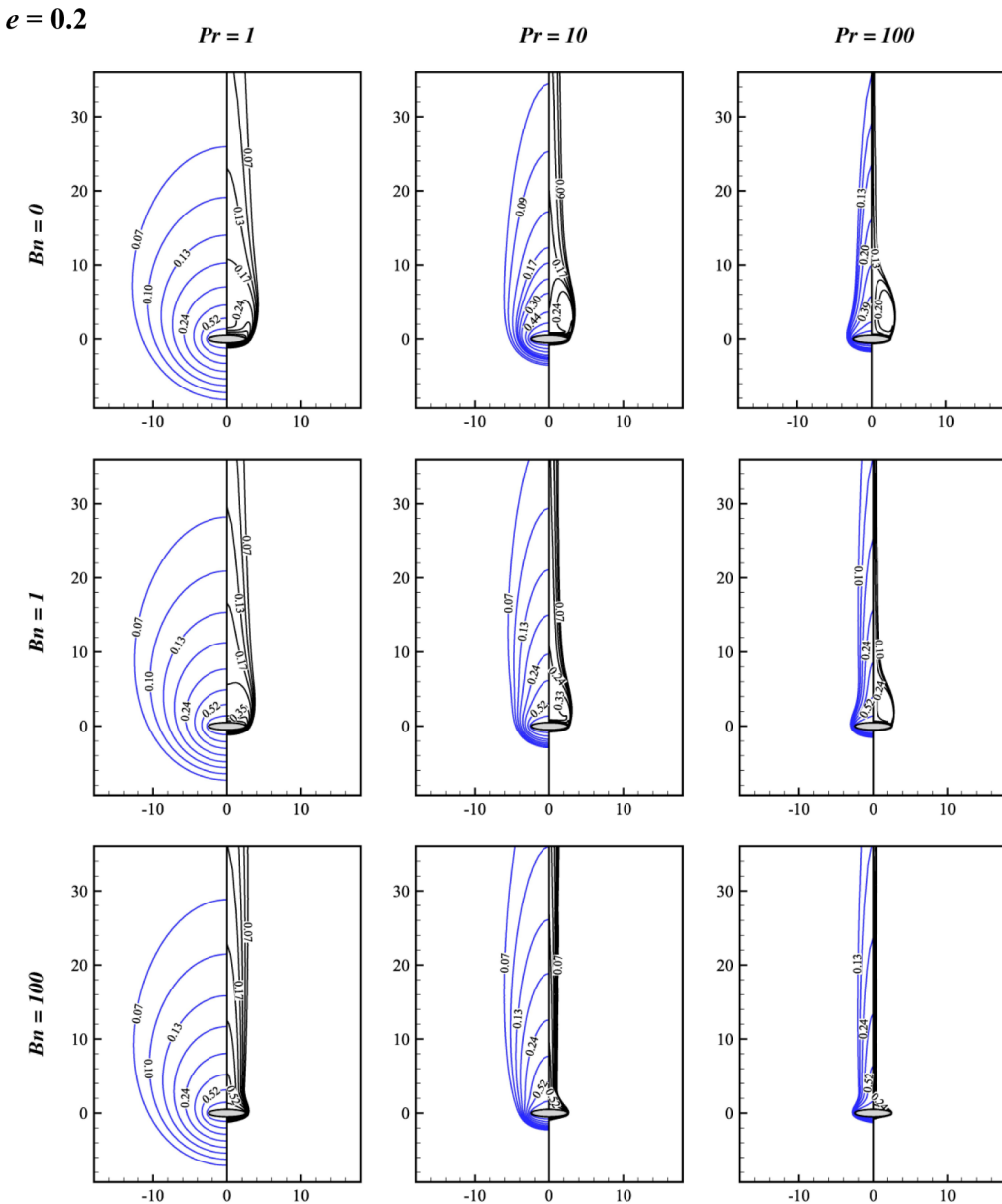


**Figure 12.** Representative isotherm contours for  $e = 0.2$  at  $Re = 1$  (left half) and  $Re = 100$  (right half).

**4.4. Velocity and Shear Rate Profiles.** From another vantage point, it is worthwhile to visualize the structure of the flow field in terms of the magnitudes of the velocity and shear rate profiles in the vicinity of the submerged spheroids. Figures 8 and 9 show the variation of the axial velocity component ( $V_y$ ) along the  $x$ - and  $y$ -axes for the extreme values of the Reynolds number,  $Re = 1$  and  $Re = 100$ , for a range of Bingham numbers and for two representative values of the aspect ratio ( $e = 0.2$  and 5). At low Reynolds numbers (e.g.,  $Re = 1$ ), the spatial decay of the  $y$ -component of the velocity in the  $x$ - and  $y$ -directions is mainly determined by the shape of the spheroid, as the fluid inertia is small under these conditions. For  $e = 0.2$ , when the major axis of the spheroid is oriented normal to the direction of mean flow, the magnitude of the velocity progressively increases monotonically from its zero value on the surface of the spheroid, eventually approaching its asymptotic value of unity as far as the Newtonian fluids are concerned. In this case, the shape of the spheroid mainly influences the rate of approach to the free stream conditions; that is, for  $e = 0.2$ , this

value is only about  $(V_y/U_\infty) \sim 0.9$  at  $x = 15$  whereas  $(V_y/U_\infty)$  is found to approach this value at about  $x = 3$  for a sphere and at about  $x \approx 1$  for  $e = 5$ . At high Reynolds numbers, the behavior is qualitatively similar in Newtonian fluids except for the fact that spatial decay becomes faster accompanied by a slight overshoot in velocity, especially in the case of less streamlined shape (such as  $e = 0.2$ , Figure 8) whereas, for  $e = 1$  and  $e = 5$ , such an overshoot is hardly visible, though not shown here for a sphere but available elsewhere.<sup>13</sup> Next, turning our attention to the variation of the  $y$ -velocity in the direction of the flow (i.e.,  $y$ -direction), at low Reynolds numbers such as at  $Re = 1$ , when no flow separation is observed, the velocity monotonically approaches its asymptotic value; once again, the rate of approach increases with the increasing degree of streamlining, i.e., with the increasing value of  $e$ . On the other hand, at high Reynolds numbers such as at  $Re = 100$ , when some shapes are conducive to flow separation, the velocity attains small negative values corresponding to the wake region; for example, see Figure 8a for  $e = 0.2$  before turning upward to approach the

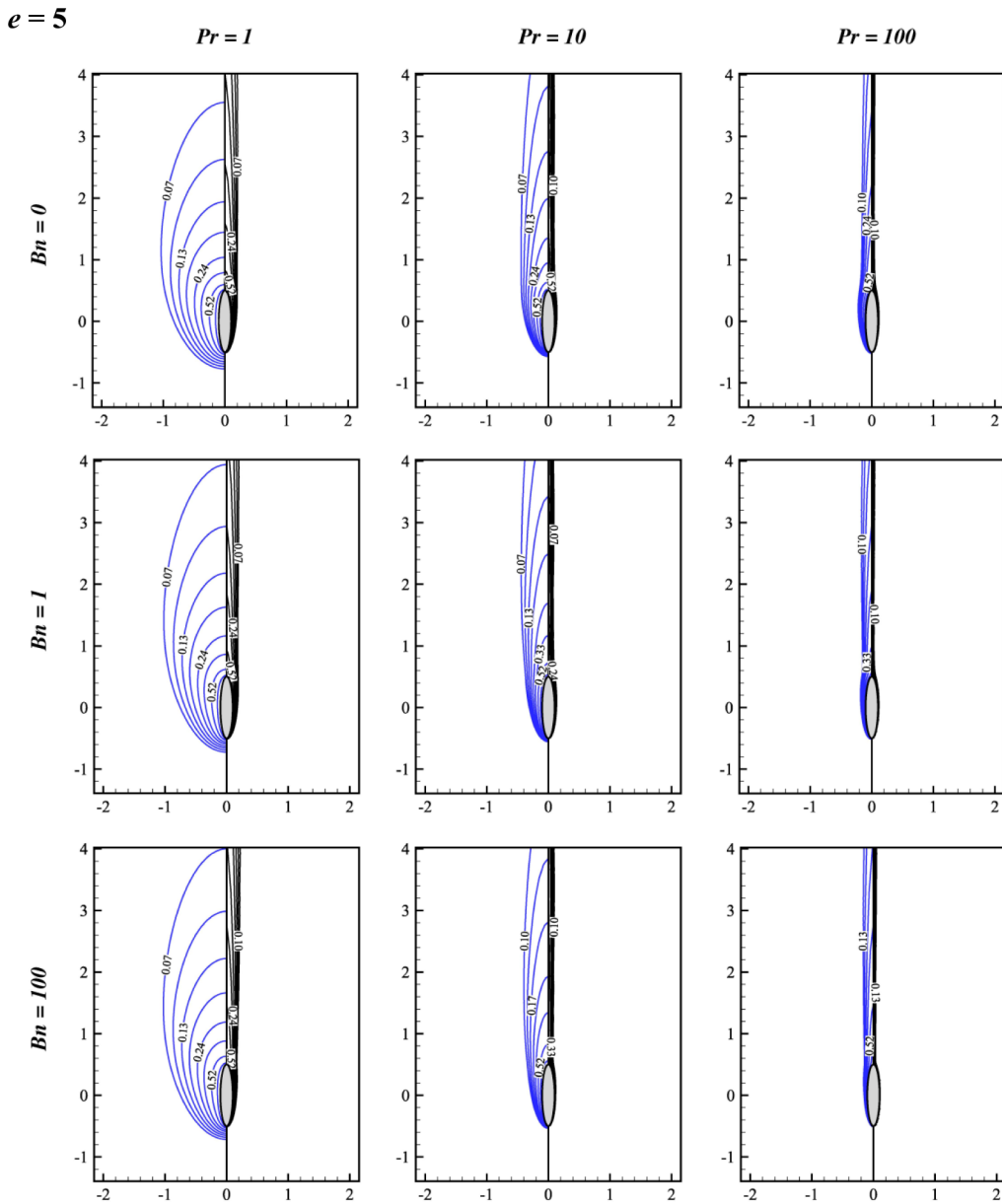


**Figure 13.** Representative isotherm contours for  $e = 5$  at  $Re = 1$  (left half) and  $Re = 100$  (right half).

expected value of unity. The rate of approach to the far field uniform flow is seen to be strongly influenced by the presence of a wake, as can be clearly seen in Figure 8b at  $Re = 1$  (no wake) and at  $Re = 100$  for Newtonian fluids ( $Bn = 0$ ). Thus, for instance, at  $y = 30$ ,  $V_y = 0.84$  at  $Re = 1$  but the corresponding value is only about 0.65–0.70 even at  $y = 50$  at  $Re = 100$ . However, since no flow separation occurs for a spheroid of  $e = 5$  even at  $Re = 100$ , no negative velocity is seen in this case (Figure 9b). Now turning our attention to the analogous results in Bingham plastic fluids, since the yield stress suppresses the propensity for flow separation (seen in streamline plots in Figures 6 and 7), only in a few cases, much smaller negative velocities are seen here due to this reason. On the other hand, due to the spheroid being encapsulated in a body of unyielded material, much bigger overshoots are observed here in the case of the variation of the  $y$ -velocity along the  $x$ -direction which are nearly independent of the value of the Reynolds number but are strongly influenced by the shape of the spheroid; for example, see Figures 8a and 9a for finite values of the Bingham

number. This is due to the requirement of the conservation of mass principle. Generally, the size of the yielded zone diminishes with the increasing Bingham number, where greater overshoot is observed at high Bingham numbers. On the other hand, the spatial decay in the  $y$ -direction becomes steeper with the increasing Bingham number, thereby leading to high levels of shearing on this count. In this case also, the shape of the spheroid exerts an appreciable influence on the nature of the velocity decay. Broadly, the faraway constant velocity segments correspond to the *en masse* uniform flow of the unyielded material. Depending upon the shape of the spheroid, the velocity can take different routes to increase from its zero value on the surface of the spheroid to the free stream velocity. Thus, for a spheroid of  $e = 0.2$ , as noted above, it increases rapidly in the  $x$ -direction from zero, overshoots beyond unity, and quickly settles down at the asymptotic value of unity. On the other hand, for a sphere ( $e = 1$ ), due to the polar caps present, there is another twist which manifests in terms of change of slope at the interface of the unyielded polar caps (undergoing rigid body

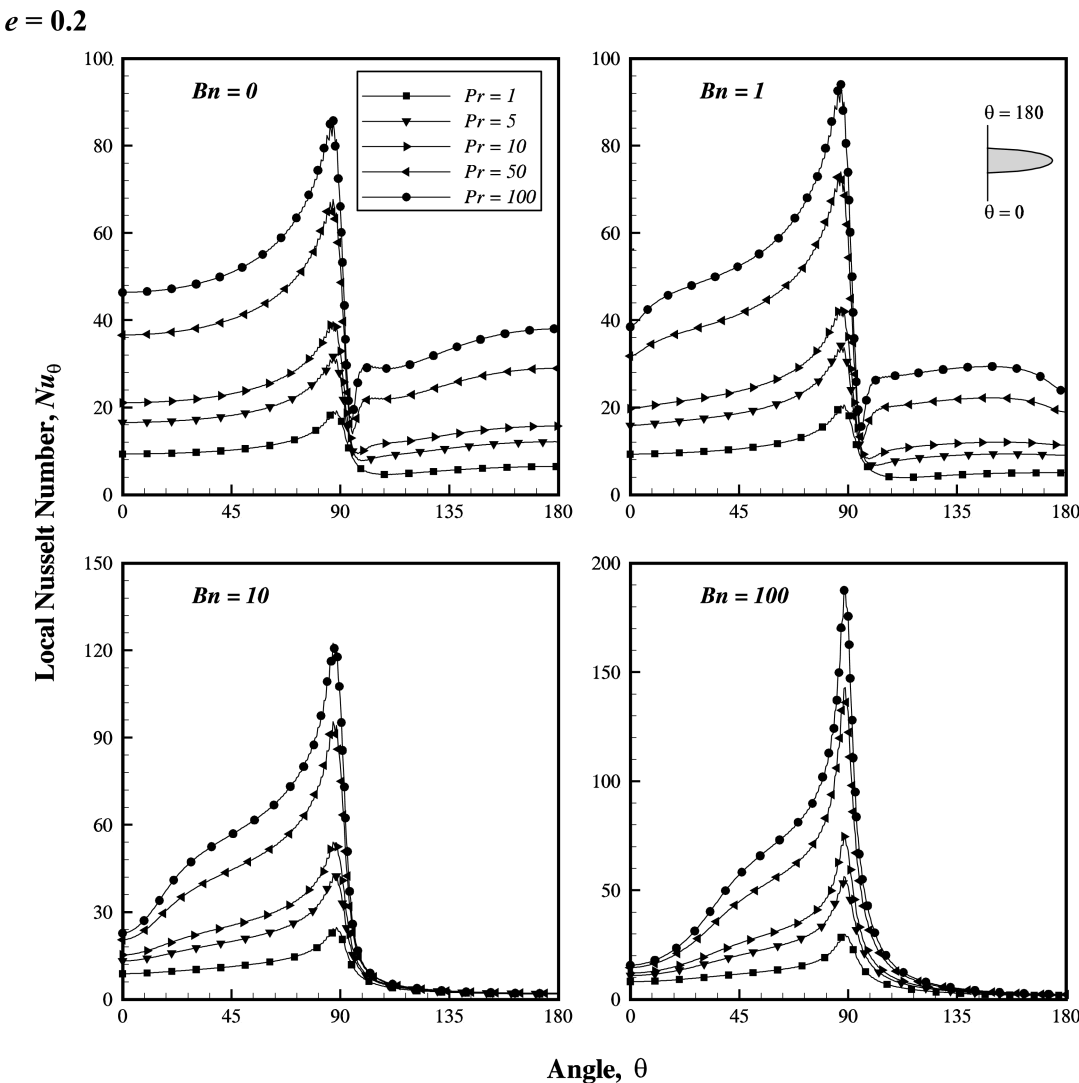


**Figure 14.** Variation of the local Nusselt number along the surface of the spheroid for  $e = 0.2$  at  $Re = 100$  ( $\theta = 0$  represents the front stagnation point).

rotation)/yielded material interface, and it rapidly decreases again to settle down to its expected value of unity,<sup>13,14</sup> whereas for slender/highly streamlined spheroids ( $e > 1$ ), there is hardly any overshoot observed and the curves are seen to be even steeper. In its most general form, one can identify four different segments, namely,  $ab$ ,  $bc$ ,  $cd$ , and  $de$  (marked in these figures), with some of these being altogether absent depending upon the value of the aspect ratio,  $e$ , as far as the variation of the  $y$ -velocity in the  $x$ -direction is concerned. For instance, as the aspect ratio of the spheroid decreases accompanied by the transition from a prolate to an oblate, segment  $bc$  becomes shorter and shorter and ultimately it vanishes altogether for the reasons outlined above. Thus, only segments  $ab$ ,  $cd$ , and  $de$  are observed in the case of  $e = 0.2$  (see Figure 8). Similarly, the variation along the  $y$ -axis ( $x = 0, y > 0$ ) is characterized in terms of three distinct segments; namely,  $ab$ ,  $bc$ , and  $cd$  irrespective of the value of Bingham number spanned here. The segment  $ab$  represents the static polar caps adhering to the rear side of the spheroid in the case of Bingham plastic fluids and it corresponds to the formation of a wake in the form of two counter rotating vortices, as indicated by the negative values of the velocity at  $Re = 100$  in Newtonian and/or by very small values

of  $Bn$  (Figure 8). Furthermore, the segment  $bc$  shows the high shear rate zone, which is dynamic in nature where the velocity changes from 0 to the free stream value of  $U_\infty$ . Finally, the segment  $cd$  indicates the outer rigid envelope, which moves en masse like a plug with a constant velocity,  $U_\infty$ . The shape of the spheroid also influences the formation of these segments quantitatively. As the aspect ratio increases, the static zone (segment  $ab$ ) decreases in size, and finally, it disappears altogether for  $e > 1$ .

Some additional insights can be gained by examining the contour plot of shear rate magnitude (Figure 10). As noted earlier, the fluid-like zones are always located very close to the surface of the spheroid irrespective of the aspect ratio, and this is revealed by very high magnitude of shear rate in the close vicinity of the object. The shear rates are seen to drop rapidly in both directions, but especially so in the transverse direction, particularly for  $e > 1$  due to the thinner momentum boundary layers than that for  $e < 1$ . This further elucidates the strong interplay between the shape of the object and the kinematic parameters. Broadly, the rate of deformation in the fluid bears a positive dependence on the Bingham number (due to shrinking yielded layer); one can thus conjecture the corresponding rate

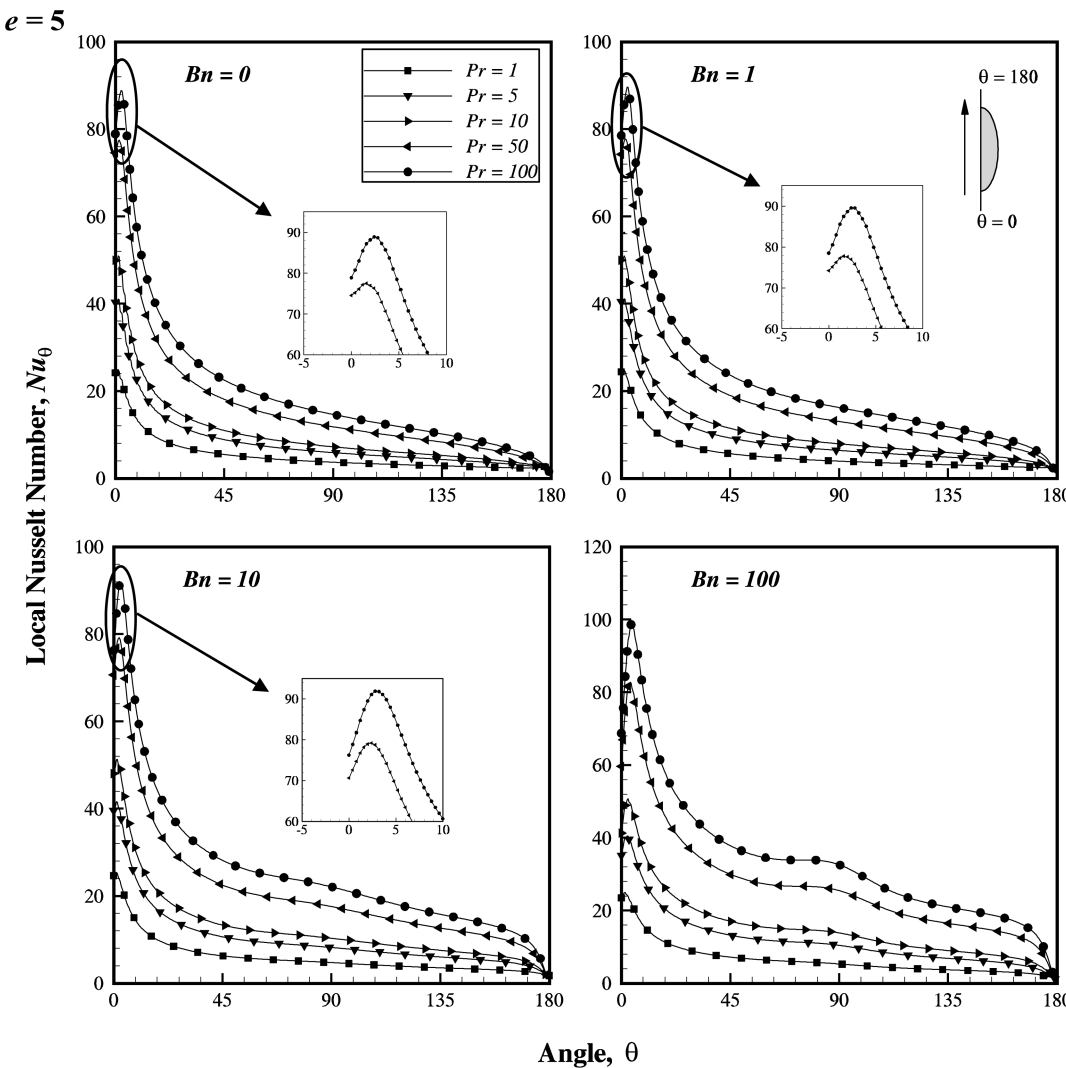


**Figure 15.** Variation of the local Nusselt number along the surface of the spheroid for  $e = 5$  at  $Re = 100$  ( $\theta = 0$  represents the front stagnation point).

of heat transfer and drag coefficient to be higher in Bingham plastic fluids than that in Newtonian fluids ( $Bn = 0$ ). At constant values of the Reynolds and Bingham numbers, the high shear zones (yielded) grow in size as the aspect ratio of the spheroid changes progressively from a prolate ( $e > 1$ ) to an oblate ( $e < 1$ ) as is borne out by the shear rate magnitude contours shown in Figure 10.

**4.5. Drag Coefficients.** Due to the prevailing shearing and normal stresses, the total drag coefficient ( $C_D$ ) is made up of two contributions, namely, viscous drag ( $C_{DF}$ ) and form or pressure drag ( $C_{DP}$ ). Figure 11 shows the dependence of the total and pressure drag coefficient on the Reynolds and Bingham numbers for a range of values of the aspect ratio. Both the total and pressure drag coefficients are seen to conform to the expected inverse dependence on the Reynolds number for a fixed value of the Bingham number. Due to the sharpening of the velocity gradients on the surface of the spheroid, both are seen to increase with the Bingham number. Furthermore, the scaling of  $C_D \sim Re^{-1}$  and  $C_{DP} \sim Re^{-1}$  is seen to extend all the way up to  $Re \sim 100$  at high Bingham numbers in contrast to the slight curvature seen in Newtonian and/or weakly viscoplastic media. This suggests the ratio ( $C_{DP}/C_D$ ) (and hence ( $C_{DP}/C_{DF}$ )) to remain almost constant at high Bingham numbers, which is indeed well borne out by the results shown in the

bottom row in Figure 11. On the other hand, as the yield stress effects weaken with the decreasing Bingham number, this ratio, ( $C_{DP}/C_{DF}$ ), is seen to increase beyond a value of the Reynolds number, which is somewhat dependent on the value of  $e$ . For blunt shapes such as  $e = 0.2$ , form drag constitutes an increasing part of the total drag and therefore as high values of ( $C_{DP}/C_{DF}$ ) as 6 are seen in contrast to the values of order  $\sim 1$  for  $e = 5$ . Following the success of the modified Reynolds number ( $Re^*$ ) in correlating the experimental and numerical drag results for a sphere,<sup>13–16</sup> the results shown in Figure 11 were replotted to check the applicability of the modified Reynolds number in the present case too. Indeed, the use of  $Re^*$  does consolidate the total and pressure drag coefficients for different values of the Bingham number onto a single curve, with exhibiting overall qualitatively similar features as noted above with reference to the Reynolds number  $Re$ . Finally, it is desirable to correlate the present numerical data using simple forms of expression. In fact, the literature is devoid of such a predictive formula for spheroids even in Newtonian fluids. The present 175 data points for  $Bn = 0$  are first approximated by modifying the well-known Schiller–Naumann drag expression<sup>24</sup> as follows:

$$C_D = \frac{24}{Re} (1 + 0.15 Re^{0.687}) e^{a_0} \quad (22)$$

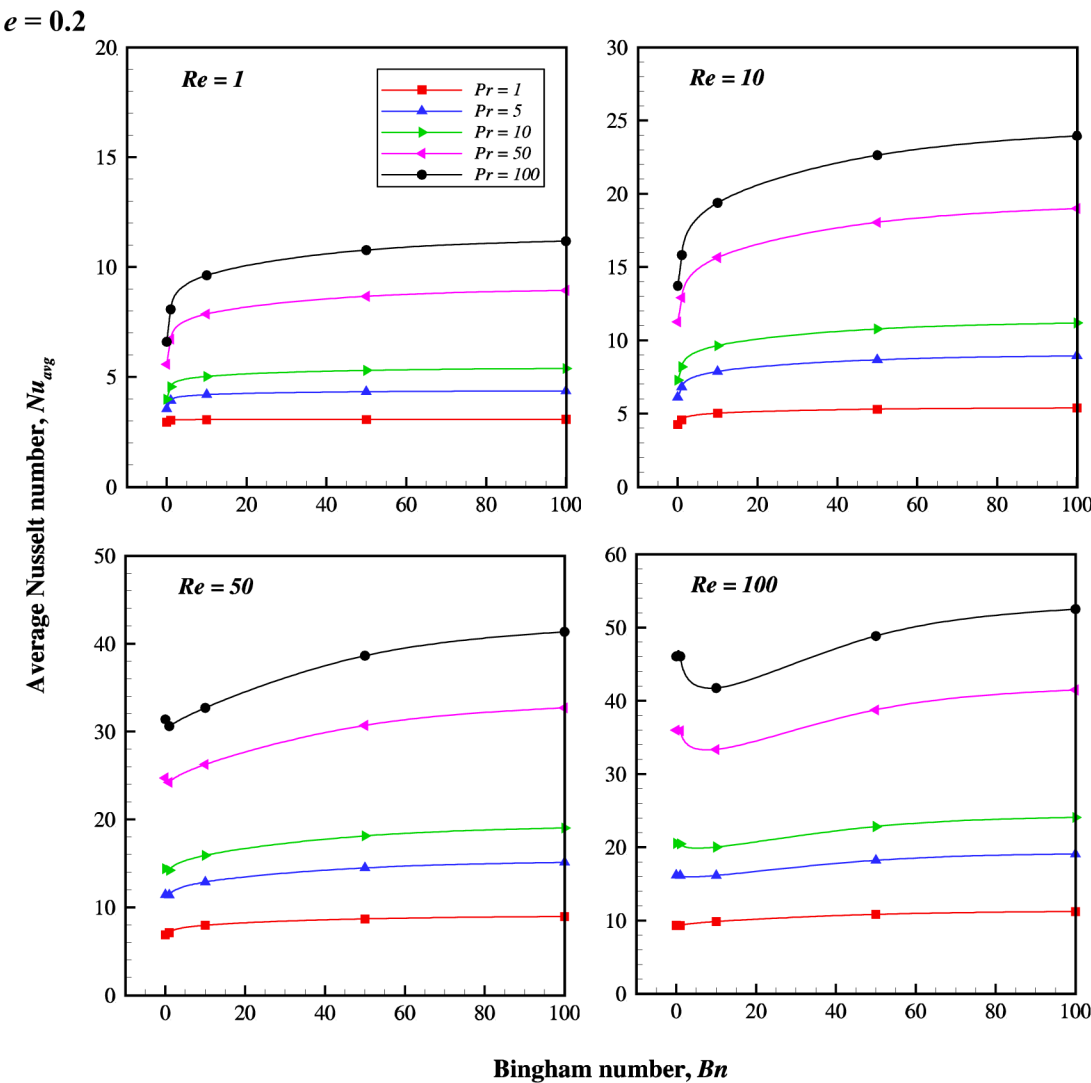


**Figure 16.** Effect of the Reynolds number ( $Re$ ), Prandtl number ( $Pr$ ), and Bingham number ( $Bn$ ) on the average Nusselt number for  $e = 0.2$ .

Naturally, for a sphere,  $e = 1$ , eq 22 reduces to the Schiller–Naumann drag expression. For  $e < 1$ , the value of  $a_o = 0.107$  reproduces the present results with a mean error of 8%, which reaches the maximum value of 23.6%. Similarly, for  $e > 1$ , the value of  $a_o = 0.379$  leads to the corresponding mean and maximum errors of 7% and 25.5%, respectively. Suffice it to say here that these orders of error are comparable to that associated with the correlation of Militzer et al.,<sup>30</sup> which contains more fitting parameters than eq 22. Now turning our attention to the drag results in Bingham plastic fluids ( $Re^* < 100; Bn^* \leq 0.99$ ), eq 22 is modified as

$$C_D = \frac{24}{Re^*} (1 + b_o Re^{*C_o}) \quad (23)$$

The resulting values of  $b_o$  and  $c_o$  together with the corresponding mean and maximum errors are summarized in Table 4. Both  $b_o$  and  $c_o$  exhibit a regular well behaved dependence on the aspect ratio,  $e$ ; albeit, the resulting average and maximum errors are larger than that seen in the case of Newtonian fluids. Further attempts to improve the degree of fit even after introducing an additional adjustable parameter proved to be unsuccessful.

**4.6. Isotherm Contours.** Representative isotherm plots are presented in Figures 12 and 13 at  $Re = 1$  (left half) and  $Re = 100$

(right half) for a range of Prandtl numbers, Bingham numbers, and aspect ratios ( $e = 0.2$  and  $e = 5$ ). The key trends can be summarized as follows. Broadly, at low Reynolds numbers and/or Prandtl numbers, the convection is weak and isotherms more or less follow the body shape, thereby indicating the dominance of the conduction mechanism. Similarly, at high Bingham numbers, much of the fluid is unyielded and once again conduction dominates under these conditions. In Newtonian fluids, as the Reynolds number and/or Prandtl number are increased, isotherms are seen to be distorted, especially downstream of the spheroids due to the flow separation and/or augmented convection. On the other hand, in viscoplastic fluids, since the yield stress suppresses fluid deformation and the tendency for flow separation, isotherms are seen to be less distorted than that in Newtonian fluids. Aside from this, the crowding of isotherms is seen to occur with the increasing values of the Prandtl number or the Reynolds number or both irrespective of the type of fluid or the shape due to the gradual thinning of the thermal boundary layer. However, the temperature field close to the surface of a heated spheroid is directly influenced by the presence of the yielded/unyielded regions. Naturally, heat transfer occurs principally by convection in such yielded domains whereas conduction dominates the heat

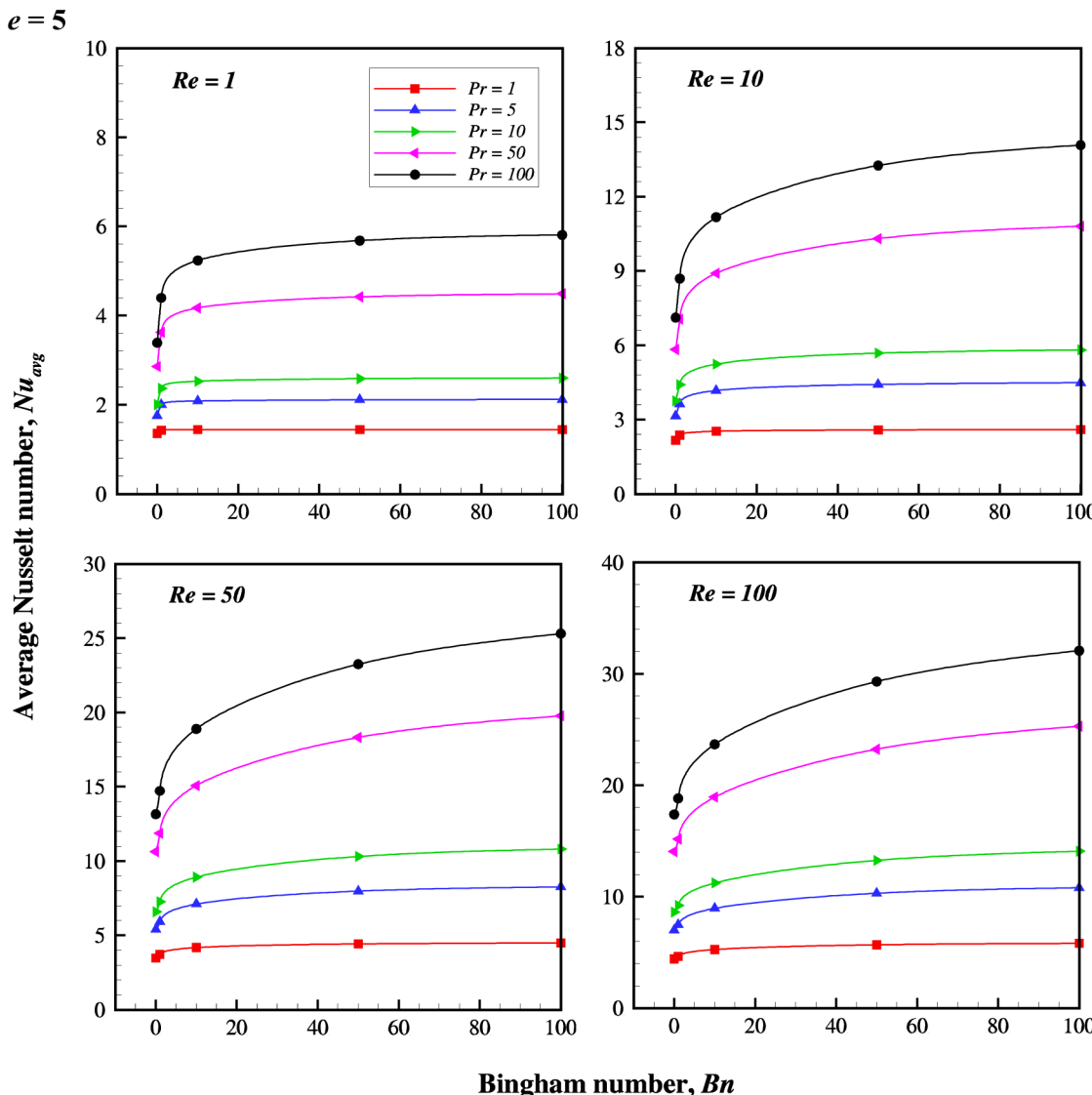


Figure 17. Effect of the Reynolds number ( $Re$ ), Prandtl number ( $Pr$ ), and Bingham number ( $Bn$ ) on the average Nusselt number for  $e = 5$ .

transport in unyielded parts (solid-like regions). So in the steady state situations such as that considered here, conduction determines the overall rate of heat transfer. Due to the gradual thinning of the thermal boundary layer with the increasing  $Bn$  values, heat transfer is expected to be higher on the frontal side than that on the rear side of the spheroid. For a fixed value of the Prandtl number, isotherm contours cluster together close to the spheroid surface with the increasing Bingham number irrespective of the aspect ratio due to the yielding being limited to a very thin layer adjacent to the spheroid surface. Thus, it is fair to postulate that the Nusselt number should exhibit a positive dependence on the Reynolds and Prandtl numbers due to the thinning of the thermal boundary layer within the framework of the classical boundary layer theory<sup>45</sup> and on the Bingham number due to the diminishing yielded regions. Indeed, these conjectures are well supported by the Nusselt number results presented and discussed in the next section.

**4.7. Local Nusselt Number Variation over the Spheroid Surface.** Despite the fact that the surface of the spheroid is maintained at a constant temperature, the temperature gradient normal to the surface of the spheroid varies from point to point due to the existing velocity and temperature

fields in the close proximity of the spheroid. Thus, the effective fluid viscosity varies along the surface of the spheroid. Such a variation in shear rate along the surface is of no relevance in the context of Newtonian fluids. Notwithstanding these complexities, typical results of the local Nusselt number distribution over the surface of the heated spheroid are presented in Figures 14 and 15 at  $Re = 100$  for a range of values of the Prandtl and Bingham numbers for an oblate and a prolate shaped spheroid. It is useful to begin with the case of a sphere (results not shown here, but available in ref 13) in a Newtonian fluid for which the maximum value of the local Nusselt number occurs at the front stagnation point ( $\theta = 0$ ) and the Nusselt number decreases until the point of flow separation ( $\theta \approx 128^\circ$  for a sphere). Beyond this point, due to the recirculation of the fluid in the rear region, the local Nusselt number somewhat increases up to the rear stagnation point. For a sphere in Bingham plastic fluids, no separation occurs and therefore no recovery is seen in the rear. Nor does the local Nusselt number exhibit its maximum value at the front stagnation point. At small Bingham numbers ( $Bn = 1$ ), the location of the maximum Nusselt number is displaced slightly downstream depending upon the value of the Prandtl number. On the other hand, at Bingham number values close to the fully

plastic flow regime, the Nusselt number exhibits two distinct peaks. These results are consistent with that reported in the literature for a sphere.<sup>13,14</sup> However, for an oblate, due to its major axis being oriented normal to the free stream, the fluid flow is somewhat impeded and heat transfer gradually increases from its minimum value at the front stagnation point, attaining its maximum value at about  $\theta = 90$  due to the abrupt bending of isotherms to follow the body contour, and in the rear of the spheroid, the local Nusselt number shows little variation due to the presence of the unyielded regions. On the other hand, in the case of a prolate, the local Nusselt number decreases much more steeply than that in the case of a sphere from its maximum value close to or at the front stagnation point to the rear stagnation point. This variation is similar to the boundary layer flow along an isothermal plate, except for a small peak slightly away from  $\theta = 0$  at high Prandtl numbers which is caused by the opposing effects of the thinning of the boundary layer due to high Prandtl number vis-a-vis the formation of the unyielding regions. At low Prandtl numbers, such regions are possibly fully inside the thick thermal boundary layer, and therefore, the maximum Nusselt number is observed at  $\theta = 0$ . Apart from these salient features, the local Nusselt number exhibits, as postulated above, a positive dependence on the Reynolds number, Prandtl number, and Bingham number for a given shape. On the other hand, for fixed values of  $Re$ ,  $Pr$ , and  $Bn$ , the local Nusselt number increases as the value of  $e$  is progressively reduced.

**4.8. Average Nusselt Number.** It is readily acknowledged that the mean values of the Nusselt number are frequently required in process engineering and design calculations. Dimensional considerations of the present situation suggest the average Nusselt number to be a function of four pertinent parameters, namely,  $Re$ ,  $Pr$ ,  $Bn$ , and  $e$  as follows:

$$Nu_{avg} = f(Re, Bn, Pr, e) \quad (24)$$

At the outset, it is worthwhile to summarize, at least qualitatively, the effects of each of these parameters on the average value of the Nusselt number. Irrespective of the values of  $Bn$  and  $e$ , the average Nusselt number shows a positive dependence on both the Reynolds number and the Prandtl number (Figures 16 and 17). This is clearly due to the progressive thinning of the momentum and thermal boundary layers. Conversely, for given values of  $Re$ ,  $Pr$ , and  $e$ , the average Nusselt number increases with the Bingham number, but it levels off at a fixed value consistent with the fully plastic flow. In addition to this, for given values of  $Re$ ,  $Bn$ , and  $Pr$ , the shape of the spheroid also influences the average Nusselt number. In general, oblates ( $e < 1$ ) facilitate heat transfer while prolates are found to yield lower Nusselt numbers consistent with the streamline and isotherm contours seen in Figures 6 and 7 and Figures 12 and 13, respectively. As the bluntness of the body shape increases, at higher values of the Reynolds number ( $Re = 100$ ), the average Nusselt number first decreases up to small values of the Bingham number and then turns upward to increase as  $Bn$  is increased further. This is simply due to the formation of the unyielded polar caps (see Figure 16). For enhancing the utility of the numerical results presented herein, it is desirable to develop a predictive expression for the average Nusselt number. Following the strategies employed in our previous studies,<sup>13,14</sup> it is advantageous to use the modified definitions of the Reynolds ( $Re^*$ ) and Prandtl ( $Pr^*$ ) numbers, thereby eliminating the explicit dependence of the average Nusselt number on the Bingham number as follows:

$$Nu_{avg} = f(Re^*, Pr^*, e) \quad (25)$$

However, this approach will still yield a family of curves depending upon the values of  $Pr^*$  and  $e$ . Further consolidation of the present results is possible by postulating the widely accepted scaling of  $Nu_{avg} \sim Pr^{*1/3}$ , thereby introducing the Colburn  $j_H$  factor as

$$j_H = \frac{Nu_{avg}}{Re^* Pr^{*1/3}} = f(Re^*, e) \quad (26)$$

For a fixed value of  $e$ , eq 26 implies the collapse of heat transfer data onto a single curve irrespective of the values of  $Pr^*$ , as can be seen in Figure 18. Based on this observation combined with

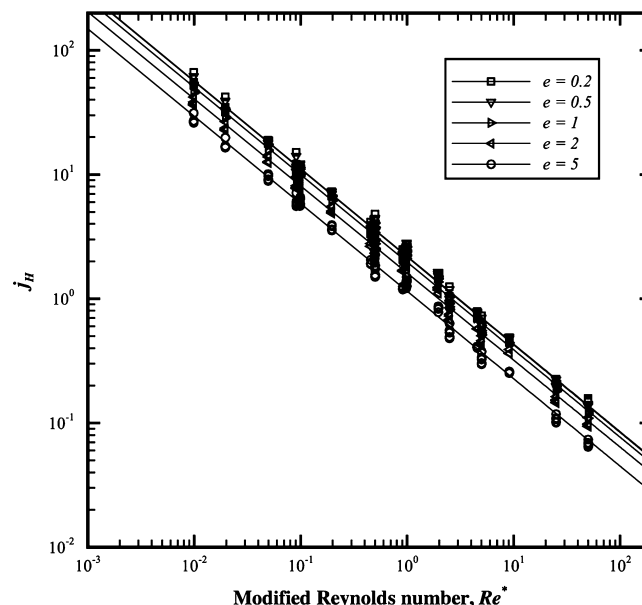


Figure 18. Dependence of the Colburn  $j_H$  factor on the modified Reynolds number ( $Re^*$ ) for a range of the values of the aspect ratio ( $e$ ).

the fact that  $j_H$  scales as  $Re^{-2/3}$  in Newtonian fluids, it is reasonable to postulate that this functional relationship for spheroids can be developed as follows:

$$j_H \cdot Re^{*2/3} = a_1 \quad (27)$$

where  $a_1$  is a constant and it is expected to be a function of the shape of the spheroid only, as summarized in Table 5. Clearly, a single set of values of  $a_1$  could not approximate the data adequately over the whole range of  $Re^*$  and/or including the Newtonian results. By trial and error, the data set was categorized into two subsets using  $Re^* = 0.5$  as the boundary between the two subsets. The single fitting constant  $a_1$  shows a regular variation with the aspect ratio,  $e$ . While the average errors in using eq 27 are typically less than ~16%, but the maximum errors are up to ~39%, which is similar to that for drag correlation discussed in the preceding sections. Further attempts to improve the degree of fit were unsuccessful. On the other hand, for Newtonian fluids ( $Bn = 0$ ), it is possible to modify the well-known Whitaker's formula<sup>46</sup> for heat transfer from a sphere as

$$Nu_{avg} = Nu_{cond} + Pr^{0.4} [x_1 Re^{1/2} + x_2 Re^{2/3}] \quad (28)$$

In the limit of  $Re \rightarrow 0$ , eq 28 correctly reduces to the limiting Nusselt number for pure conduction, i.e.,  $Nu_{cond} = 2$  for a

**Table 5.** Value of Constant ( $a_1$ ) Used in Eq 27 for  $Bn > 0$ 

Range	Aspect ratio ( $e$ )	$a_1$	% Error	
			Mean	Max.
$9.9 \times 10^{-3} \leq Re^* < 0.5$	0.2	2.55	8.85	29.4
	0.5	2.47	6.36	18.8
	1	2.18	6.69	15.6
	2	1.75	6.71	17.0
	5	1.27	6.31	14.5
$0.5 \leq Re^* < 100$	0.2	2.2	12.3	39.5
	0.5	2.25	15.0	35.9
	1	2.02	16.1	39.2
	2	1.66	15.4	35.6
	5	1.2	15.6	38.8

**Table 6.** Constants of Eq 28 with the Corresponding Errors for  $Bn = 0$  (Newtonian Fluids)

$e$	$Nu_{cond}$	$x_1$	$x_2$	% Error	
				Mean	Max.
0.2	2.63	-0.055	0.447	4.3	19.9
0.5	2.4	-0.084	0.477	5.3	20.7
1	2	0.40	0.06	6.1	17.0
2	1.54	-0.089	0.388	6.5	20.7
5	1.07	-0.067	0.278	9.0	22.8

sphere ( $e = 1$ ). The values of the constants of eq 28, i.e.,  $x_1$ ,  $x_2$ , and  $Nu_{cond}$  and the corresponding errors are summarized in Table 6. In contrast to the fitting parameters in previous equations, the values of  $x_1$  and  $x_2$  appearing in eq 28 show rather unusual irregular dependence on the aspect ratio,  $e$ , of the spheroid, especially for the limiting case of the sphere. While this makes the interpolation of these results for the intermediate values of aspect ratio,  $e$ , rather difficult, it is believed to stem from the rather large number of the pertinent dimensionless parameters here and the nonlinear form of the fitted expression. This difficulty is further accentuated by the desire to include the limiting cases of pure conduction and/or the case of a sphere, and perhaps due to the limited results for the intermediate values of the Reynolds number, Prandtl number, etc. In spite of these intrinsic difficulties, eq 28 approximates the present data in Newtonian fluids over the ranges  $1 \leq Re \leq 100$ ,  $1 \leq Pr \leq 100$ , and  $0.2 \leq e \leq 5$ . Suffice it to add here that the limiting conduction Nusselt number,  $Nu_{cond}$ , for spheroids used here is in line with the analytical values available in the literature.<sup>47</sup>

Finally, a comment about the maximum errors mentioned above is in order. While the seemingly large maximum errors of ~40% associated with eqs 27 and 28 are discomforting, given the complexity of the problem in terms of the number of dimensionless groups involved here and their ranges spanned, it is far from straightforward to correlate these data. Therefore, bearing in mind the simplicity of eq 27, this level of correlation is regarded to be satisfactory and acceptable.

## 5. CONCLUSIONS

In this work, the forced convection momentum and heat transfer characteristics of an isothermal spheroid in a Bingham plastic fluid have been investigated numerically over the following ranges of conditions:  $1 \leq Re \leq 100$ ;  $1 \leq Pr \leq 100$ ;  $0 \leq Bn \leq 100$ ; and  $0.2 \leq e \leq 5$ . Extensive results elucidating the effect of each of these parameters on the streamline and isotherm contours in the proximity of the spheroid as well as in

terms of the yielded/unyielded regions are discussed in detail. Broadly, for fixed values of the Bingham number and aspect ratio of the spheroid, the crowding of streamlines and isotherms occurs with the increasing Reynolds and Prandtl numbers due to the gradual thinning of the boundary layers, thereby sharpening the velocity and temperature gradients. Also, the size of the yielded fluid-like domain increases with the rising Reynolds number whereas this tendency is somewhat offset by the increasing Bingham number. This also leads to the sharpening of gradients. The simultaneous coexistence of such yielded and unyielded subdomains influences the extent of mixing and local temperature field, thereby influencing the overall heat transfer in such systems. On either count, the drag coefficient shows a positive dependence on the Bingham number for a given Reynolds number and aspect ratio,  $e$ . Similarly, the Nusselt number bears a positive correlation with both the Reynolds and Prandtl numbers but the effect of shape is more intricate. Broadly, all else being equal, blunt shapes ( $e < 1$ ) facilitate convective heat transport whereas streamlined shapes ( $e > 1$ ) are less conductive to heat transfer. Also, as the streamlining in the body increases the tendency of wake formation is reduced. The present numerical results on drag and Nusselt number (in the form of  $j_H$  factor) have been correlated satisfactorily with the modified Reynolds and Prandtl numbers incorporating the effect of the Bingham number. Indeed, such correlations for spheroids are not available even in Newtonian media. For the latter, the well-known existing drag and Nusselt number correlations for a sphere have been suitably modified by incorporating the effect of shape. However, owing to the too many dimensionless parameters, the correlations presented herein entail maximum errors of up to ~40%. This not only suggests a complex interplay between the shape and the kinematic parameters in determining the drag and Nusselt number values, but also makes it far from being straightforward to postulate the most suitable form of such correlations. In spite of these limitations, the predictive expressions presented here do seem to capture the essence of this functional relationship.

## ■ ASSOCIATED CONTENT

### Supporting Information

Detailed results showing the choice of optimum numerical parameters (domain, grid, value of  $m$ ) and additional validation details. This material is available free of charge via the Internet at <http://pubs.acs.org/>.

## ■ AUTHOR INFORMATION

### Corresponding Author

\*Phone: +91 512 2597393. Fax: +91 512 2590104. E-mail: chhabra@iitk.ac.in.

### Notes

The authors declare no competing financial interest.

## ■ NOMENCLATURE

$a$  = spheroid semiaxis normal to flow, m

$A_p$  = projected area of spheroid normal to the flow,  $\text{m}^2$

$b$  = spheroid semiaxis parallel to the flow, m

$Bn$  = Bingham number ( $\equiv \tau_o(2a)/\mu_B U_\infty$ ), dimensionless

$C$  = heat capacity of the fluid,  $\text{J}\cdot\text{kg}^{-1}\cdot\text{K}^{-1}$

$C_D$  = total drag coefficient ( $\equiv 2F_D/\rho U_\infty^2 A_p$ ), dimensionless

$C_{DF}$  = friction drag coefficient ( $\equiv 2F_{DF}/\rho U_\infty^2 A_p$ ), dimensionless

$C_{DP}$  = pressure drag coefficient ( $\equiv 2F_{DP}/\rho U_\infty^2 A_p$ ), dimensionless  
 $C_p$  = pressure coefficient ( $\equiv 2(p_w - p_\infty)/\rho U_\infty^2$ ), dimensionless  
 $D_\infty$  = diameter of the computational domain, m  
 $e$  = aspect ratio of spheroid ( $\equiv b/a$ ), dimensionless  
 $F_D$  = drag force, N  
 $F_{DF}$  = frictional component of drag force, N  
 $F_{DP}$  = pressure component of drag force, N  
 $h$  = heat transfer coefficient, W·m<sup>-2</sup>·K<sup>-1</sup>  
 $j_H$  = Colburn  $j$ -factor, dimensionless  
 $k$  = thermal conductivity of the fluid, W·m<sup>-1</sup>·K<sup>-1</sup>  
 $m$  = growth rate parameter, dimensionless  
 $n_s$  = unit normal vector on the surface of a spheroid, dimensionless  
 $N_p$  = number of grid points on spheroid surface, dimensionless  
 $Nu_{avg}$  = average Nusselt number, dimensionless  
 $Nu_{cond}$  = conduction limit of the Nusselt number for a spheroid, dimensionless  
 $Nu_\theta$  = local Nusselt number, dimensionless  
 $p$  = pressure, dimensionless  
 $Pr$  = Prandtl number ( $\equiv \mu_B C/k$ ), dimensionless  
 $Pr^*$  = modified Prandtl number [ $\equiv Pr(1 + Bn)$ ], dimensionless  
 $Re$  = Reynolds number ( $\equiv 2aU_\infty\rho/\mu_B$ ), dimensionless  
 $Re^*$  = modified Reynolds number [ $\equiv Re/(1 + Bn)$ ], dimensionless  
 $S$  = surface area of spheroid, m<sup>2</sup>  
 $T$  = temperature of fluid, K  
 $U_\infty$  = uniform inlet velocity, m·s<sup>-1</sup>  
 $V$  = velocity vector, dimensionless  
 $V_x$  = velocity component in  $x$ -direction, dimensionless  
 $V_y$  = velocity component in  $y$ -direction, dimensionless  
 $x, y$  = Cartesian coordinates, dimensionless

### Greek Symbols

$\dot{\gamma}$  = rate of deformation tensor, dimensionless  
 $|\dot{\gamma}|$  = magnitude of the rate of deformation tensor, dimensionless  
 $\eta$  = apparent viscosity, dimensionless  
 $\theta$  = position on the surface of spheroid, deg  
 $\varphi$  = temperature ( $\equiv (T - T_\infty)/(T_w - T_\infty)$ ), dimensionless  
 $\mu_B$  = plastic viscosity, Pa·s  
 $\mu_y$  = yielding viscosity, Pa·s  
 $\rho$  = density of the fluid, kg·m<sup>-3</sup>  
 $\tau$  = deviatoric stress tensor, dimensionless  
 $\tau_o$  = yield stress of the fluid, Pa  
 $|\tau|$  = magnitude of deviatoric stress tensor, dimensionless

### Subscripts

$w$  = condition at spheroid surface  
 $\infty$  = condition far away from spheroid

## ■ REFERENCES

- Bird, R. B.; Dai, G. C.; Yarusso, B. J. The rheology and flow of viscoplastic materials. *Rev. Chem. Eng.* **1983**, *1*, 1–70.
- Barnes, H. A. 1999. The yield stress—a review or ‘παντα ρε’—everything flows? *J. Non-Newt. Fluid Mech.* **1999**, *81*, 133–178.
- Balmforth, N. J.; Frigaard, I. A.; Ovarlez, G. Yielding to stress: Recent developments in viscoplastic fluid mechanics. *Annu. Rev. Fluid Mech.* **2014**, *46*, 121–146.
- Lawal, A.; Mujumdar, A. S. Laminar duct flow and heat transfer. *Transport Phenomena in Polymeric Systems-1*; Wiley: Eastern Delhi, 1987, 352–444.
- Chhabra, R. P.; Richardson, J. F. *Non-Newtonian Fluid and Applied Rheology: Engineering Applications*, 2<sup>nd</sup> ed.; Butterworth-Heinemann: Oxford, 2008.
- Chhabra, R. P.; Comiti, J.; Machac, I. Flow of non-Newtonian fluids in fixed and fluidised beds: a review. *Chem. Eng. Sci.* **2001**, *56*, 1–27.
- Chhabra, R. P. *Bubbles, Drops and Particles in Non-Newtonian Fluids*, 2<sup>nd</sup> ed.; CRC Press: Boca Raton, 2006.
- Paul, E. L.; Atiemo-Obeng, V. A.; Kresta, S. M. *Handbook of Industrial Mixing: Science and Practice*; Wiley: Hoboken, NJ, 2004.
- Chhabra, R. P. Fluid mechanics and heat transfer with non-Newtonian liquids in mechanically agitated vessels. *Adv. Heat Transfer* **2003**, *37*, 77–178.
- Beris, A. N.; Tsamopoulos, J. A.; Armstrong, R. C.; Brown, R. A. Creeping motion of a sphere through a Bingham plastic. *J. Fluid Mech.* **1985**, *158*, 219–244.
- Beaulne, M.; Mitsoulis, E. Creeping motion of a sphere in tubes filled with Herschel-Bulkley fluids. *J. Non-Newt. Fluid Mech.* **1997**, *72*, 55–71.
- Blackery, J.; Mitsoulis, E. Creeping motion of a sphere in tubes filled with a Bingham plastic material. *J. Non-Newt. Fluid Mech.* **1997**, *70*, 59–77.
- Nirmalkar, N.; Chhabra, R. P.; Poole, R. J. Numerical predictions of momentum and heat transfer characteristics from a heated sphere in yield-stress fluids. *Ind. Eng. Chem. Res.* **2013**, *52*, 6848–6861.
- Nirmalkar, N.; Chhabra, R. P.; Poole, R. J. Effect of shear-thinning behaviour on heat transfer from a heated sphere in yield-stress fluids. *Ind. Eng. Chem. Res.* **2013**, *52*, 13490–13504.
- Atapattu, D. D.; Chhabra, R. P.; Uhlherr, P. H. T. Creeping sphere motion in Herschel-Bulkley fluids: flow field and drag. *J. Non-Newt. Fluid Mech.* **1995**, *59*, 245–265.
- Atapattu, D. D.; Chhabra, R. P.; Uhlherr, P. H. T. Wall effects for spheres falling at small Eynolds number in a viscoplastic medium. *J. Non-Newt. Fluid Mech.* **1990**, *38*, 31–42.
- Tabuteau, H.; Coussot, P.; de Bruyn, J. R. Drag force on a sphere in steady motion through a yield-stress fluid. *J. Rheol.* **2007**, *51*, 125–137.
- Gumulya, M. M.; Horsley, R. R.; Wilson, K. C.; Pareek, V. A new fluid model for particle settling in a viscoplastic fluid. *Chem. Eng. Sci.* **2011**, *66*, 729–739.
- Hariharaputhiran, M.; Subramanian, R. S.; Campbell, G. A.; Chhabra, R. P. The settling of spheres in a viscoplastic fluid. *J. Non-Newt. Fluid Mech.* **1998**, *79*, 87–97.
- Prashant; Derkens, J. J. Direct simulations of spherical particle motion in Bingham liquids. *Comput. Chem. Eng.* **2011**, *35*, 1200–1214.
- Yu, Z.; Wachs, A. A fictitious domain method for dynamic simulation of particle sedimentation in Bingham fluids. *J. Non-Newt. Fluid Mech.* **2007**, *145*, 78–91.
- Nirmalkar, N.; Chhabra, R. P. Momentum and heat transfer from a heated circular cylinder in Bingham plastic fluids. *Int. J. Heat Mass Transfer* **2014**, *70*, 564–577.
- Patel, S. A.; Chhabra, R. P. Heat transfer in Bingham plastic fluids from a heated elliptical cylinder. *Int. J. Heat Mass Transfer* **2014**, *73*, 671–692.
- Clift, R.; Grace, J. R.; Weber, M. E. *Bubbles, Drops and Particles*; Academic Press: New York, 1978.
- Michaelides, E. E. *Particles, Bubbles and Drops: Their Motion, Heat and Mass Transfer*; World Scientific: Singapore, 2006.
- Kishore, N.; Gu, S. Wall effects on flow and drag phenomena of spheroid particles at moderate Reynolds numbers. *Ind. Eng. Chem. Res.* **2010**, *49*, 9486–9495.
- Kishore, N. Flow and drag phenomena of tandem spheroid particles at finite Reynolds numbers. *Ind. Eng. Chem. Res.* **2012**, *51*, 3186–3196.
- Kishore, N.; Gu, S. Momentum and heat transfer phenomena of spheroid particles at moderate Reynolds and Prandtl numbers. *Int. J. Heat Mass Transfer* **2011**, *54*, 2595–2601.

- (29) Kishore, N.; Gu, S. Effect of blockage on heat transfer phenomena of spheroid particles at moderate Reynolds and Prandtl numbers. *Chem. Eng. Technol.* **2011**, *34*, 1551–1558.
- (30) Militzer, J.; Kan, J. M.; Hamdullahpur, F.; Amyotte, P. R.; Al Taweel, A. M. Drag coefficient for axisymmetric flow around individual spheroidal particles. *Powder Technol.* **1989**, *57*, 193–195.
- (31) Tripathi, A.; Chhabra, R. P.; Sundararajan, T. Power law fluid flow over spheroidal particles. *Ind. Eng. Chem. Res.* **1994**, *33*, 403–410.
- (32) Tripathi, A.; Chhabra, R. P. Drag on spheroidal particles in dilatant fluids. *AICHE J.* **1995**, *41*, 728–731.
- (33) Sreenivasulu, B.; Srinivas, B.; Ramesh, K. V. Forced convection heat transfer from a spheroid to a power-law fluid. *Int. J. Heat Mass Transfer* **2014**, *70*, 71–80.
- (34) Song, D.; Gupta, R. K.; Chhabra, R. P. Heat transfer to a sphere in tube flow of power-law liquids. *Int. J. Heat Mass Transfer* **2012**, *55*, 2110–2121.
- (35) Song, D.; Gupta, R. K.; Chhabra, R. P. Effect of blockage on heat transfer from a sphere in power-law fluids. *Ind. Eng. Chem. Res.* **2010**, *49*, 3849–3861.
- (36) Dhole, S. D.; Chhabra, R. P.; Eswaran, V. Forced convection heat transfer from a sphere to non-Newtonian power law fluids. *AICHE J.* **2006**, *52*, 3658–3667.
- (37) Suresh, K.; Kannan, A. Effect of particle diameter and position on hydrodynamics around a confined sphere. *Ind. Eng. Chem. Res.* **2011**, *50*, 13137–13160.
- (38) Suresh, K.; Kannan, A. Effect of particle blockage and eccentricity in location on the non-Newtonian fluid hydrodynamics around a sphere. *Ind. Eng. Chem. Res.* **2012**, *51*, 14867–14883.
- (39) Glowinski, R.; Wachs, A. On the numerical simulation of viscoplastic fluid flow. In *Handbook of Numerical Analysis*; Glowinski, R., Xu, J., Eds.; Elsevier: North-Holland, 2011; pp 483–717.
- (40) Papanastasiou, T. C. Flow of materials with yield. *J. Rheol.* **1987**, *31*, 385–404.
- (41) O' Donovan, E. J.; Tanner, R. I. Numerical study of the Bingham squeeze film problem. *J. Non-Newt. Fluid Mech.* **1984**, *15*, 75–83.
- (42) Liu, B. T.; Muller, S. J.; Denn, M. M. Convergence of a regularization method for creeping flow of a Bingham material about a rigid sphere. *J. Non-Newt. Fluid Mech.* **2002**, *102*, 179–191.
- (43) Masliyah, J. H.; Epstein, N. Numerical study of steady flow past spheroids. *J. Fluid Mech.* **1970**, *44*, 493–512.
- (44) Zamyshlyaev, A. A.; Shrager, G. R. Fluid flows past spheroids at moderate Reynolds numbers. *Fluid Dyn.* **2004**, *39*, 376–383.
- (45) Schlichting, H.; Gersten, K. *Boundary-Layer Theory*; McGraw-Hill: New York, 1960.
- (46) Whitaker, S. Forced convection heat transfer correlations for flow in pipes, past flat plates, single cylinders, single spheres and flow in packed beds and tube bundles. *AICHE J.* **1972**, *18*, 361–371.
- (47) Alassar, R. S. Heat conduction from spheroids. *J. Heat Transfer* **1999**, *121*, 497–499.